Search for a new boson W' in the electron plus missing transverse momentum final state using 2017 CMS data at $\sqrt{s} = 13\,\text{TeV}$

von
Steffen Coenen

Bachelorarbeit in Physik

vorgelegt der
Fakultät für Mathematik, Informatik und Naturwissenschaften der RWTH Aachen University

im August 2018

angefertigt am
III. Physikalischen Institut A
bei
Prof. Dr. Thomas Hebbeker
Zweitgutachter
Prof. Dr. Christopher Wiebusch

Zentrales Prüfungsamt/Central Examination Office

Eidesstattliche Versicherung
Statutory Declaration in Lieu of an Oath

Name, Vorname/Last Name, First Name

Matrikelnummer (freiwillige Angabe)
Matriculation No. (optional)

Ich versichere hiermit an Eides Statt, dass ich die vorliegende Arbeit/Bachelorarbeit/ Masterarbeit* mit dem Titel
I hereby declare in lieu of an oath that I have completed the present paper/Bachelor thesis/Master thesis* entitled

selbstständig und ohne unzulässige fremde Hilfe (insbes. akademisches Ghostwriting) erbracht habe. Ich habe keine anderen als die angegebenen Quellen und Hilfsmittel benutzt. Für den Fall, dass die Arbeit zusätzlich auf einem Datenträger eingereicht wird, erkläre ich, dass die schriftliche und die elektronische Form vollständig übereinstimmen. Die Arbeit hat in gleicher oder ähnlicher Form noch keiner Prüfungsbehörde vorgelegen.
independently and without illegitimate assistance from third parties (such as academic ghostwriters). I have used no other than the specified sources and aids. In case that the thesis is additionally submitted in an electronic format, I declare that the written and electronic versions are fully identical. The thesis has not been submitted to any examination body in this, or similar, form.

Ort, Datum/City, Date

Unterschrift/Signature

*Nichtzutreffendes bitte streichen

*Please delete as appropriate

Belehrung:
Official Notification:

§ 156 StGB: Falsche Versicherung an Eides Statt
Wer vor einer zur Abnahme einer Versicherung an Eides Statt zuständigen Behörde eine solche Versicherung falsch abgibt oder unter Berufung auf eine solche Versicherung falsch aussagt, wird mit Freiheitsstrafe bis zu drei Jahren oder mit Geldstrafe bestraft.
Para. 156 StGB (German Criminal Code): False Statutory Declarations
Whoever before a public authority competent to administer statutory declarations falsely makes such a declaration or falsely testifies while referring to such a declaration shall be liable to imprisonment not exceeding three years or a fine.
§ 161 StGB: Fahrlässiger Falscheid; fahrlässige falsche Versicherung an Eides Statt
(1) Wenn eine der in den §§ 154 bis 156 bezeichneten Handlungen aus Fahrlässigkeit begangen worden ist, so tritt Freiheitsstrafe bis zu einem Jahr oder Geldstrafe ein.
(2) Straflosigkeit tritt ein, wenn der Täter die falsche Angabe rechtzeitig berichtigt. Die Vorschriften des § 158 Abs. 2 und 3 gelten entsprechend.
Para. 161 StGB (German Criminal Code): False Statutory Declarations Due to Negligence
(1) If a person commits one of the offences listed in sections 154 through 156 negligently the penalty shall be imprisonment not exceeding one year or a fine.
(2) The offender shall be exempt from liability if he or she corrects their false testimony in time. The provisions of section 158 (2) and (3) shall apply accordingly.

Die vorstehende Belehrung habe ich zur Kenntnis genommen:
I have read and understood the above official notification:

Ort, Datum/City, Date

Unterschrift/Signature

Abstract

In this thesis, the search for a new heavy vector boson W' in the final state with an electron and missing transverse momentum is presented. The used data is based on proton-proton collisions from 2017 at a centre-of-mass energy of $\sqrt{s} = 13\,\text{TeV}$ and is provided by the CMS experiment. It corresponds to an integrated luminosity of $41.5\,\text{fb}^{-1}$. The measurements are compared to the Standard Model background predictions and interpreted in terms of a possible new boson W'.

Using the transverse mass distribution as the discriminating variable, no significant deviation from the Standard Model prediction is observed. Thus, an exclusion limit has been set by comparing the data to simulated signal samples in the Sequential Standard Model (SSM) interpretation. Doing this, W' masses below 4.85 TeV can be excluded at a 95% confidence level.

In addition, a study on Vector Boson Fusion (VBF) processes including the production and decay of a new charged boson that can be interpreted as a W' has been performed. Signal samples are compared on a qualitative level to the findings in the SSM W' search. Despite slight differences in the kinematic distributions, the two signal types show comparable behaviour. VBF cross sections are at least two orders of magnitude smaller than for the W' production in the context of the SSM.

Kurzdarstellung

Diese Arbeit präsentiert die Suche nach einem neuen schweren Vektorboson W' in dem Endzustand mit einem Elektron und fehlendem Transversalimpuls. Die verwendeten Daten stammen von Proton-Proton-Kollisionen aus dem Jahr 2017 bei einer Schwerpunktsenergie von $\sqrt{s} = 13\,\text{TeV}$ und wurden vom CMS-Experiment bereitgestellt. Sie umfassen eine integrierte Luminosität von $41.5\,\text{fb}^{-1}$. Die Messungen werden mit der Vorhersage des Standardmodellhintergrundes verglichen und in Bezug auf ein mögliches neues Boson W' interpretiert.

Unter Benutzung der Transversalmasse als diskriminierende Variable wurden keine signifikanten Abweichungen zum Standardmodell beobachtet. Daher wurden durch Vergleich der gemessenen Daten mit simulierten Signalsätzen in der Interpretation des Sequentiellen Standardmodells Ausschlussgrenzen gesetzt. Es können W'-Massen unterhalb von 4.85 TeV auf einem 95%-Konfidenzniveau ausgeschlossen werden.

Zusätzlich werden Fusionsprozesse mit Vektorbosonen (VBF) untersucht, die die Produktion und den Zerfall eines neuen geladenen Bosons, welches als W' interpretiert werden kann, umfassen. Signalsätze werden qualitativ mit den Ergebnissen der SSM W'-Suche verglichen. Trotz leichter Unterschiede in den kinematischen Verteilungen sind beide Signaltypen vergleichbar. VBF-Wirkungsquerschnitte sind mindestens zwei Größenordnungen kleiner als für die W'-Produktion im Kontext des SSM.

Contents

1. Introduction

Considering a steadily evolving setting of priorities in all foundational sciences, physics is developing constantly and relentlessly. Despite, the field of particle physics has constantly been an important domain in the past decades – focussing either on the discovery of theoretically predicted elementary particles, gaining more knowledge on particles' properties or the understanding of the basic construction of forces in nature. The Standard Model is the product of these developments and the state of today's knowledge.

At institutions like the Large Hadron Collider (LHC) at CERN, extensions to the Standard Model are permanently under investigation. The search for a new, heavy, charged boson W' decaying into an electron and neutrino has been a key analysis in the past years [1–4]. Simple kinematic selection criteria yield a clear signature which allows for a wide range of interpretations in this decay channel. This thesis focusses on the Sequential Standard Model interpretation and Vector Boson Fusion processes.

The 2017 dataset taken at the Compact Muon Solenoid experiment at the LHC is the biggest set cumulated in one year so far. It corresponds to an integrated luminosity of $41.5\,\mathrm{fb}^{-1}$ and confronts the CMS collaboration with challenges regarding the understanding of detector properties and a proper and efficient reconstruction of particles.

In Chapter 2, this thesis begins with the construction of the theoretical framework this search is embedded in. The CMS experiment with its constituents and features is presented in Chapter 3. The samples used in this analysis are shown in Chapter 4 including actual collision data as well as simulated samples. In the following Chapter 5, general selection and identification criteria, that are put in front of analysis specific criteria, are described. These preceding remarks are the basis for the analysis flow performed for the 2017 dataset in Chapter 6. Finally, an alternative signal process involving the fusion of vector bosons is investigated as a comparative study in Chapter 7.

2. Theoretical Background

In this chapter, an introduction to the field of elementary particles will be given. This is vital for searches for physics beyond the current and generally accepted state of knowledge, that physicists call the Standard Model, or SM for short. Starting with an introduction to the Standard Model, one extension to it will be presented in the second section of this chapter, that deals with the Sequential Standard Model (SSM).

This thesis will make use of the natural unit system, unifying the dimensions of mass and energy. In the natural unit system, energies as well as masses and momenta can be given in terms of the electron volt ($1\,\mathrm{eV} = 1.60218 \times 10^{19}\,\mathrm{J}$).

The content of this chapter is selected as a basis for the analysis, but shall not be understood as a complete overview of the field of elementary particle physics.

2.1. The Standard Model

If not stated otherwise, the information contained in this section is predominantly taken from D. Griffiths' "Introduction to Elementary Particles" [5].

The Standard Model of particle physics describes all known elementary particles and their interaction based on gauge invariances. The model emerged in the 1960s and 1970s and evolved over the years leading to our current understanding of the very fundamental concepts in nature – including particles, forces, and fields. Elementary particles are extremely tiny chunks of matter that are indivisible and constituting the whole universe around us. The Standard Model represents a consistent description of the electromagnetic, weak and strong interactions in terms of the gauge group $\mathsf{U}(1)_Y \times \mathsf{SU}(2)_L \times \mathsf{SU}(3)_C$ but, in contrast, does not provide a substantial understanding of gravity. Today's idea of gravity is mainly built upon Einstein's General Theory of Relativity [6].

2.1.1. Particles

In the Standard Model, each and every particle has its unique quantum numbers, such as charge or spin. The elementary particles can be divided into two groups: the fermions (half-integer spin) and the bosons (integer spin). The latter are often called mediators, targeting their function as the interceding particles of forces.

Fermions The fermions themselves can be divided into leptons and quarks. The former interact electroweak only, whilst the latter takes also part in the strong interaction. In Table 2.1 the fermions contained in the SM are listed. Every fermion has a partner, the anti-fermion, that has all the signs of its quantum numbers reversed. For example, the positron as the electron's antiparticle carries charge +1 and electron number -1. In this thesis, the denotation of a particle always means its antiparticle, too, unless

stated otherwise. For each charged lepton there is one non-charged neutrino. In the SM, the neutrinos are massless, but at the present day, due to neutrino oscillations, it is known that they indeed have mass [7]. There are 6 different leptonic particles, each having an antiparticle, yielding a sum of 12 leptons.

The second group of fermions, the quarks, can also be divided into three generations. They reach by far higher masses than the leptons and form hadrons like the proton or the neutron. In total, there are 6 quarks and 6 anti-quarks.

Table 2.1.: The fermions of the Standard Model. Each particle listed here has an antiparticle as its partner. The uncertainties on the light quarks' masses are substantial. Based on [8].

	generation	particle	name	mass	charge
leptons	1	e^-	electron	0.511 MeV	-1
		ν_e	electron neutrino	< 2 eV	0
	2	μ^-	muon	106 MeV	-1
		ν_μ	muon neutrino	< 2 eV	0
	3	τ^-	tau	1777 MeV	-1
		ν_τ	tau neutrino	< 2 eV	0
quarks	1	u	up	2.2 MeV	$+2/3$
		d	down	4.7 MeV	$-1/3$
	2	c	charm	1.27 GeV	$+2/3$
		s	strange	0.096 GeV	$-1/3$
	3	t	top	173 GeV	$+2/3$
		b	bottom	4.18 GeV	$-1/3$

Bosons The bosons have integer spin and are the mediators of particle-particle interactions. The photon (γ) mediates the electromagnetic force, and it is massless. Thus, its range is infinite. The weak force is mediated by the $\mathsf{W}^\pm$ and the Z^0 vector bosons. Additionally, for the strong interaction there are in total eight gluons, corresponding to different colour combinations (see Section 2.1.3). Furthermore, there may be a potential "graviton" for the gravitational force but this is not part of the Standard Model and has not been found until this day. Table 2.2 lists the bosons with some of their properties. The Higgs boson was found in 2012 [9, 10] and is the most recently discovered elementary particle.

2.1.2. Interactions

As mentioned separately before, there are four fundamental forces in nature, see Table 2.3. The first three are contained within the Standard Model and described via quantum field theories (QFT). In QFT, particles are treated as excited states of physical fields, those states are being called field quanta. The electromagnetic and weak interactions are merged terminologically to the concept of electroweak interaction. That is how it is done in the Glashow-Weinberg-Salam (GWS) theory (see Section 2.1.4). In this sense, the number of fundamental interactions can be given as three.

Table 2.2.: The bosons of the Standard Model and their properties. Based on [8].

interaction mediated	particle	name	mass	electric charge
electromagnetic	γ	photon	0 GeV	0
weak	$\mathsf{W}^{\pm}$	vector boson	80.39 GeV	± 1
	Z^0		91.19 GeV	0
strong	g	gluon	0 GeV	0
electroweak symmetry breaking	H	Higgs	125.09 GeV	0

Table 2.3.: The known four fundamental forces in nature. The term "geometrodynamics" is taken from [5] and displays an alternative for "theory of relativity". The strength is an ambiguous notion, it actually depends on the nature of the source and the distance to it.

interaction	strength	theory	mediator
strong	10	quantum chromodynamics	gluon g
electromagnetic	10^{-2}	electrodynamics	photon γ
weak	10^{-13}	flavordynamics	W and Z
gravitational	10^{-42}	geometrodynamics	(graviton)

2.1.3. Quantum Chromodynamics – Strong Interaction

This thesis is about the analysis of events from a hadron collider, so the understanding of the strong interaction is vital to conceive the contribution of some background samples. The theory of Quantum Chromodynamics (QCD) deals with the strong interaction, in which only quarks participate. Quarks have a colour charge: red, blue, or green. QCD is characterized by the gauge group $\mathsf{SU}(3)$ and there are eight physically possible ways to arrange gauge fields, corresponding to the eight gluons of the SM as the mediators of the strong interaction. Each gluon is distinctly defined by a combination of the three colour charges. The force range of the gluons is finite, and the coupling strength α_s rises with increasing distance of the interacting quarks, which is called confinement. A still increasing distance between the quarks increases the system's energy. This leads to the point where enough energy is available to create new quark-antiquark pairs ($E = mc^2$). As a consequence of this ongoing so-called hadronisation, parton showers occur which can be observed as jets in a modern particle detector. Bound states are always colourless. Colourless combinations can be constructed by a quark-antiquark pair (mesons) or three quarks containing all colours (baryons, like the proton), despite other possible, but less likely combinations.

2.1.4. Quantum Electrodynamics and Flavordynamics – Electroweak Interaction

Quantum Electrodynamics (QED) was the first SM interaction theory to be developed. The mediator of the corresponding electromagnetic interaction is the photon, being massless and without self-coupling. Hence, the range of the electromagnetic force is infinite.

The last fundamental interaction to mention is the weak force, mediated by the three gauge bosons $\mathsf{W}^{\pm}$ and Z^0. Due to their mass (see for Table 2.2) the range of this interaction is heavily limited to the order of about 10^{-18} m. The W-boson production and decay will be the main background of the data in this analysis.

Electrodynamics and the weak interaction can be merged to form the so-called Electroweak Interaction. This unification was proposed and urged by Glashow, Weinberg and Salam, e. g. [11]. The corresponding gauge group is a combination of the electromagnetic group $\mathsf{U}(1)_Y$ and the weak group $\mathsf{SU}(2)_L$ to $\mathsf{SU}(2)_L \times \mathsf{U}(1)_Y$. This group is linked to four massless fields; two charged fields (W^1 and W^2) and two neutral fields (W^3 and B). The bosons of the electromagnetic (γ) and weak ($\mathsf{W}^{\pm}$, Z^0) interaction are produced as mixed states of these bosons of the electroweak interaction.

2.1.5. Higgs Mechanism

Demanding local gauge invariance one needs to add an additional field to the Standard Model in order to fulfil this requirement. This field, the Higgs field, implies a new massive scalar particle, the Higgs particle. It couples to the gauge bosons giving them their mass. This mechanism was firstly introduced in 1964 by Peter Higgs and François Englert [12, 13] and in 2012 the Higgs boson was finally discovered by the experiments at the LHC. The masses of the quarks and leptons of the SM can be explained via a further interaction, called Yukawa coupling.

2.2. The Sequential Standard Model

The Standard Model is understood and tested very well. Many experiments and studies lead to results matching accurately to the SM. Nevertheless, the Standard Model cannot embody the (whole) truth as in fact there are some experimental results either in contradiction to it or not being able to be explained by the SM. One example for an observation like that is the gravitational astronomy, a field in which evidence for further sources of mass than the one obtained by the Higgs field has been found [14, 15]. Another evidence for physics beyond the Standard Model (BSM) are the neutrino oscillations [7] indicating that neutrinos actually are not massless. In the Standard Model, the neutrinos do not have mass.

Some discussed and investigated extensions to the Standard Model implement heavy copies of the SM vector bosons, generally referred to as W' and Z'. The so-called "Sequential Standard Model", short SSM, as a reference model provides a generic W' for benchmark searches at current particle colliders [16]. In this thesis, the production and decay of the W' boson into the final state with an electron and a neutrino are investigated. The corresponding Feynman graph of this process is shown in Figure 2.1.

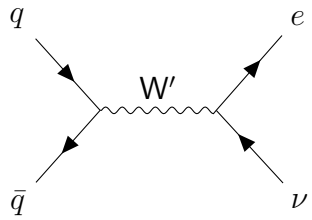

Figure 2.1.: Feynman graph of the production and decay of the SSM W' boson into an electron and neutrino. The particles in the final state could be replaced by their antiparticles, too.

The coupling of the SSM W' to fermions is assumed to be the same as for the SM W. In addition, for the expected large mass of the W' boson the decay channel $t\bar{b}$ is allowed. In some models, the ZW channel, that would be dominant for $M_{\mathsf{W}'} > 250\,\mathrm{GeV}$, is suppressed. In the SSM, the ZW coupling is assumed to be zero. Interference between SM W and SSM W' are neglected [17]. The W' is mainly produced off-shell.

The W' decay width into an electron-neutrino pair can be calculated via

$$\Gamma_{\mathsf{W}'\to f\bar{f}'} = m_{\mathsf{W}'}\frac{g^2_{\mathsf{W}'}C_{f\bar{f}'}}{2\cdot 48\pi}\,F\left(\frac{m_f}{m_{\mathsf{W}'}},\frac{m_{\bar{f}'}}{m_{\mathsf{W}'}}\right), \tag{2.1}$$

where $C_{f\bar{f}'}$ is the color factor and $g_{\mathsf{W}'}$ the W''s coupling constant [16, 17]. $C_{f\bar{f}'} = 1$ holds for leptons and $C_{f\bar{f}'} = 3$ for quarks. The correction factor

$$F(x_1,x_2) = \left[2 - x_1^2 - x_2^2 - (x_1^2 - x_2^2)^2\right]\sqrt{\left[1-(x_1+x_2)^2\right]\left[1-(x_1-x_2)^2\right]}$$

takes into account the higher mass of the W' boson compared to the fermions. As an approximation, one can set $m_f/m_{\mathsf{W}'} \approx 0$ for all fermions except the top (t) and bottom (b) quark. Then, $F(0,0) = 2$ yields for the decay width

$$\Gamma_{\mathsf{W}'\to f\bar{f}'} = m_{\mathsf{W}'}\frac{g^2_{\mathsf{W}'}}{2\cdot 48\pi}\left[18 + 3\,F\left(\frac{m_t}{m_{\mathsf{W}'}},\frac{m_b}{m_{\mathsf{W}'}}\right)\right]. \tag{2.2}$$

A further approximation is obtained for W' masses even much higher than the top mass of $m_t = 173\,\mathrm{GeV}$. In that case, Equation 2.2 simplifies to

$$\Gamma_{\mathsf{W}'\to f\bar{f}'} = m_{\mathsf{W}'}\frac{g^2_{\mathsf{W}'}}{4\pi} = \frac{4}{3}\frac{m_{\mathsf{W}'}}{m_{\mathsf{W}}}\Gamma_{\mathsf{W}},$$

assumig $g_W = g_{\mathsf{W}'}$ in the second step. It follows by the SM W decay width $\Gamma_{\mathsf{W}} = m_{\mathsf{W}}\frac{3g^2_{\mathsf{W}}}{16\pi}$ deriving from Equation 2.1. Table 2.4 shows decay widths for selected W' masses.

Table 2.4.: SSM W' decay widths for selected masses considering couplings to fermions.

mass $m_{\mathsf{W}'}$	decay width Γ
1.8 TeV	59.1 GeV
3.8 TeV	124.7 GeV
5.0 TeV	164.1 GeV

3. The CMS Experiment

3.1. The Large Hadron Collider at CERN

The Large Hadron Collider (LHC) is a high energy particle accelerator and collider and is located near Geneva in Switzerland. It is the world's most powerful accelerator complex regarding aspects like beam energy and instantaneous luminosity [18]. It consists of a 26.7-kilometre-long ring between 45 and 170 m below the surface being surrounded by superconducting magnets for acceleration and focussing purposes [19].

The collider ring is placed inside the tunnel that was originally built for the Large Electron-Positron Collider (LEP). Starting with first ideas of a hadron collider inside the LEP tunnel in 1984, the planning of the LHC was approved by the CERN Council in 1994. The LEP experiment was launched in 1989 but closed again in 2000 to start modifying preparations for the LHC.

The LHC is built for proton-proton acceleration and collisions at centre-of-mass energies up to 14 TeV. The protons are focussed longitudinally and transversely into bunches, packages of up to $11 \cdot 10^{10}$ particles. A second mode of operation enables heavy ion collisions (lead-lead) at 2.8 TeV per nucleon. The peak luminosity is $10^{34}\,\mathrm{cm}^{-2}\mathrm{s}^{-1}$ for *pp* collisions and $10^{27}\,\mathrm{cm}^{-2}\mathrm{s}^{-1}$ for lead-lead collisions. The instantaneous luminosity L can be calculated with

$$L = \frac{N_1 N_2 f_{\mathrm{rev}} N_b}{4\pi\sigma_x\sigma_y}\,,$$

where N_b is the number of bunches, N_1 and N_2 are the number of particles (at LHC: protons) per bunch and f_{rev} the revolution frequency. σ_x and σ_y describe the transverse vagueness of the bunches. Usually one assumes gaussian bunch shapes (beam profiles) with standard deviations $\sigma_{x,y}$. Additional factors can be applied on the luminosity in order to consider a potential crossing angles or other beam profiles. One can obtain the integrated luminosity $\mathcal{L}$ as a measure for the total achieved beam crossing intensity by integrating over time,

$$\mathcal{L} = \int_{\mathrm{runtime}} L\,\mathrm{d}t\,.$$

Figure 3.1 shows an overview of the whole CERN site. There are several experiments installed, four of them are connected to the LHC. Firstly, there is the "Large Hadron Collider beauty" (LHCb), which deals with b hadrons and their decay. Other experiments belonging to LHC are "A Lare Ion Collider Experiment" (ALICE) (investigates on lead-lead collisions) and A Toroidal LHC Apparatus (ATLAS). Finally, there is the "Compact Muon Solenoid" (CMS), the experiment taking the data used in this analysis. It is described further in the following Section 3.2.

The protons circulating in the LHC are taken from a hydrogen gas which is ionized by the use of strong electric fields to strip off the electron from each atomic core. The protons are injected into the PS Booster (in the figure BOOSTER) with an energy

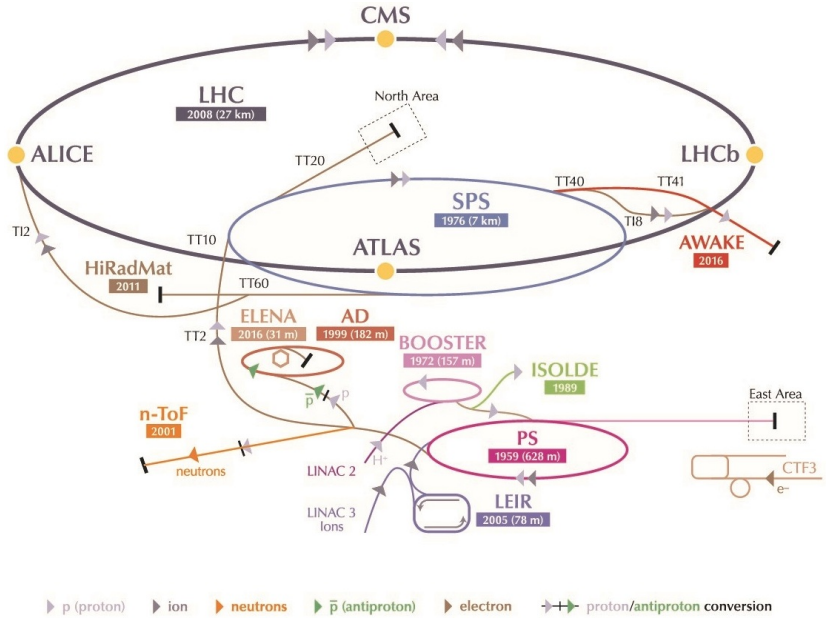

Figure 3.1.: A schematic overview on the CERN accelerator complex. One can see the different experiments and accelerators with their name and year of initial operation. Taken from [20].

of about 50 MeV after being pre-accelerated in a linear accelerator (LINAC2). The booster increases the proton energy to 1.4 GeV and then feeds the particles to the Proton Synchrotron (PS). From that, they are sent to the Super Proton Synchrotron (SPS) reaching 450 GeV. Finally, they get forwarded to the LHC where they again are exposed to further acceleration up to 6.5 TeV for each beam [21]. This leads to the operational centre-of-mass energy of 13 TeV.

3.2. CMS detector

The Compact Muon Solenoid (CMS) is one of the two general-purpose detectors at the LHC. It is located close to the French village of Cessy about 100 metres underground. It weighs about 14,000 tons and has an overall diameter of 15 m and a length of 28.7 m. CMS' purpose is to provide a good event reconstruction of the scatter products from proton-proton collisions. Hence, the detector has to fill requirements such as a good momentum resolution and reconstruction efficiency for charged particles. As already stated in its name the CMS detector also has a focus on good muon identification and momentum resolution. The energy resolution, diphoton and dielectron mass resolution, missing transverse momentum resolution are also needed to be valuable.

Given the LHC's enormous rate of one bunch crossing every 25 ns the CMS detector faces formidable experimental challenges. At design luminosity, about 10^9 events/s are expected. As this amount of data cannot be fully stored, the online event selection process, the triggers, have to harshly reduce the rate of events to about 100/s being stored for analyses. The additional fact that per crossing there are several (in mean roughly 20) collisions – this effect is called pile-up – imposes the requirement of a precise vertex reconstruction and time resolution.

The information above and many of the following is mainly based on [22].

Figure 3.2 shows a sketch of the CMS detector. Its composition concept is comparable to an onion, where different detector components are located radially around the beam axis. Therefore, the CMS Collaboration uses a coordinate system with the origin in the interaction point. Due to the cylindrical symmetry of the detector, the z axis is defined as the beam axis. The x axis points radially inward towards the centre of the LHC, the y axis vertically upward. The azimuthal angle ϕ starts from the x axis is measured in the x-y plane, where also the radial component r lies. The polar angle θ starts from the z axis.

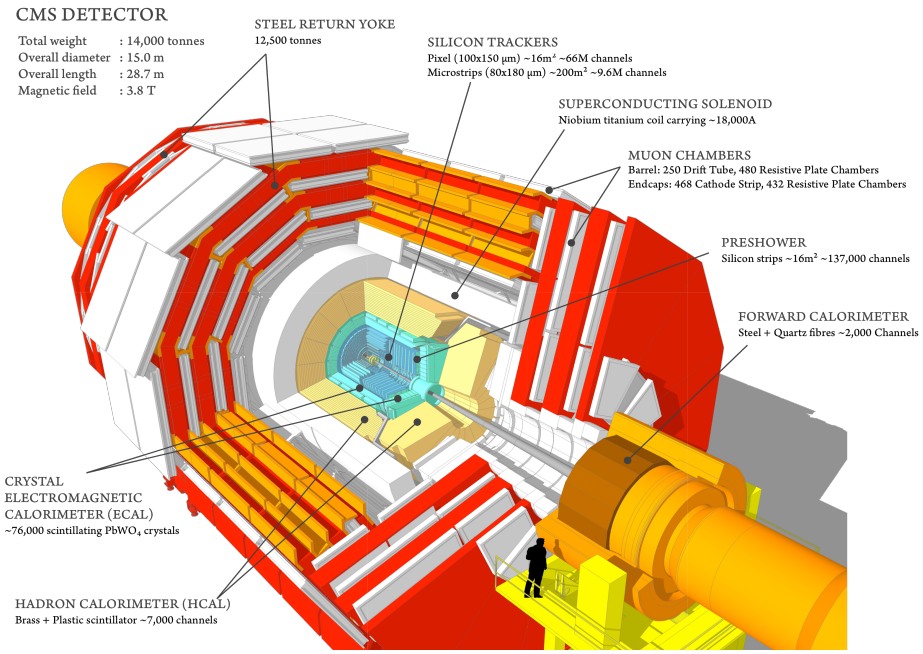

Figure 3.2.: A perspective view of the CMS detector. The beam axis (z axis) lies along the gray pipe through the middle of the detector. The interaction point of the colliding particles sits right in the middle of the sketch at the yellow marker. Taken from [23].

By that, one can define the pseudorapidity

$$\eta \equiv -\ln\left[\tan(\theta/2)\right] ,$$

which is invariant under Lorentz transformations. In Figure 3.3, one can see the relation between the two polar quantities θ and η. For θ near 0 or 180° the pseudorapidity η diverges to ∞ and $-\infty$, respectively. These two sectors near the beam axis correspond to the very forward and backward regions of the detector.

As a measure for the angular separation between two particles traversing the detector the spatial distance

$$\Delta R \equiv \sqrt{(\Delta\eta)^2 + (\Delta\phi)^2}$$

is defined. For particles with much smaller masses compared to their energy, it is Lorentz invariant. This holds for most cases in high energy studies. In addition to

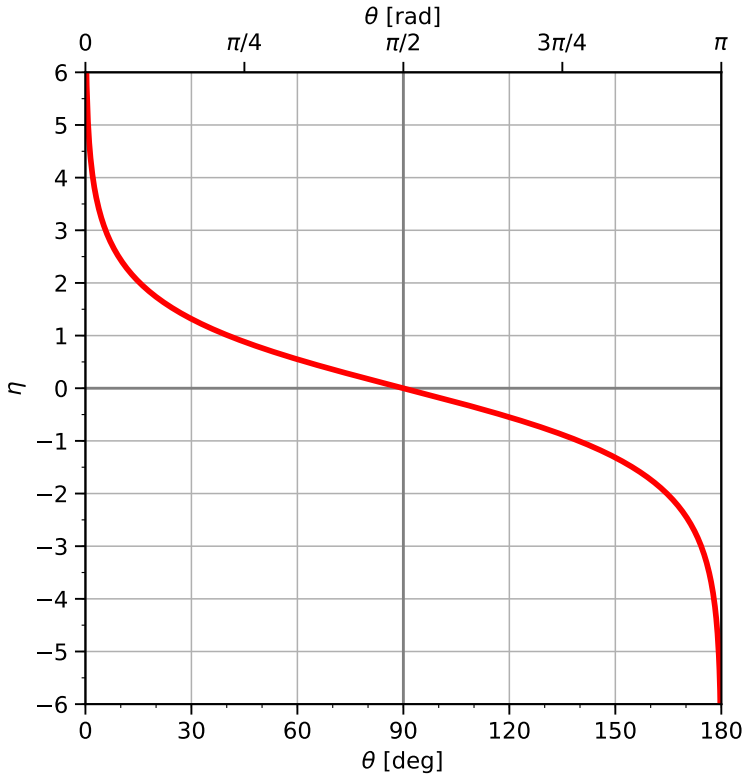

Figure 3.3.: The functional relation between θ and η. The polar angle θ is given in degrees as well as in radiant units.

that, energy and momentum transverse to the beam direction are defined as single quantities:

$$E_T = \sum^* E\,,$$
$$p_T = \sqrt{p_x^2 + p_y^2}\,,$$

where the sum marked with an asterisk (*) considers all particles with a non-negligible p_T. As being of deep interest in this analysis the transverse mass M_T of two particles $P1$ and $P2$ is defined via

$$M_T \equiv \sqrt{2p_T^{P1}p_T^{P2}\left(1 - \cos[\Delta\phi(P1, P2)]\right)}\,, \tag{3.1}$$

with the transverse momenta $p_T^{P1,P2}$ of the two particles and $\Delta\phi(P1, P2)$ the azimuthal angle between them. In Section 4.2.2, the purpose of this variable will be explained.

3.2.1. Composition

In this section, the different detector components of the Compact Muon Solenoid will be explained. If not stated otherwise, the information given in this section consolidates on [22].

Tracker

The most inner layer of the detector contains the inner tracking system. It provides a precise measurement of trajectories of charged particles as well as reconstruction capability of secondary vertices. It is 5.8 m long and 2.5 m in diameter. Different experimental challenges such as the high flux of particles through the tracker and therefore high requirements on response time and granularity imply further difficulties including the instigation of cooling systems or a finite lifetime (expected 10 years). The tracker is composed of on the one hand a pixel detector with three barrel layers with a maximum radius of 10.2 cm and on the other hand a silicon strip tracker with ten layers extending the system to a radius of about 1.1 m. The barrels are each supplemented by endcaps broadening the tracker's acceptance up to $|\eta| < 2.5$.

Calorimeters

The two calorimeters built in the CMS detector serve the purpose of energy measurements, either for electromagnetic (electrons, photons) or hadronic particle showers. They are located outside the tracker.

Electromagnetic Calorimeter (ECAL) The ECAL is made of lead tungstate crystals ($PbWO_4$) which is highly transparent and scintillates when electrons and photons pass through it. It is a high-density material making it possible to meet the demands for a fast, fine granulated and radiation resistant material. Almost 80,000 crystals split up to the barrel and endcaps covering a total pseudorapidity region of up to $|\eta| < 3.0$. Silicon avalanche photodiodes (APDs) detect the scintillation light in the barrel, whilst this is done by vacuum phototriodes (VPTs) in the endcap region. For a stable scintillation yield, the system is cooled by water to 18 °C.

Hadron Calorimeter (HCAL) The second calorimeter is built for the measurement of hadron jets or exotic particles that lead to missing transverse energy. Hadronic particles can appear in many final states. Additionally, the measurement of missing transverse energy is important due to rarely interacting particles like neutrinos. The HCAL is made of a brass scintillator material and the scintillation light is detected by hybrid photodiodes (HPDs) after being wavelength-shifted and channelled to the diodes via clear fibres. Just like the previously mentioned detector parts the HCAL is divided into a barrel and an endcap region. The barrel (HB) covers a pseudorapidity range of $|\eta| < 1.3$, the endcaps (HE) reach the region $1.3 < |\eta| < 3.0$. Furthermore, the very forward region is covered by forward calorimeters (HF).

Solenoid

The 13-m-long and 6-m-wide superconducting solenoid provides a large bending power. It has originally been designed to produce a magnetic field of 4 T, it operates with 3.8 T though. The coil axis is equivalent with the beam axis, so the magnetic field lines are perpendicular to the x-y-plane in the centre. This leads to a bending Lorentz force on charged particles with a non-zero transverse momentum component. The radius of a

particle's bent trajectory is used to determine its momentum. The solenoid marks the closure of the inner detector parts, namely the tracker, the ECAL and the HCAL.

Muon chambers

Outside of the solenoid, the muon system is located. The detection of muons is of central importance for the CMS experiment, taking into account the potential of muon final states e. g. in Higgs decay. The system is appropriate for muon identification and momentum measurement. The latter is provided over the entire kinematic range of the LHC. The barrel drift tubes (DT) cover the $|\eta| < 1.2$ region and are made of standard rectangular drift cells. They are organised into four stations. The endcap region features cathode strip chambers (CSC) having a fast response time and high radiation resistance. The whole system reaches pseudorapidity coverage up to $|\eta| < 2.4$.

3.2.2. Data-taking

Triggering The bunch crossing rate of one crossing every 25 ns, which corresponds to a frequency of 40 MHz, together with the previously mentioned pile-up effect makes it impossible to store every information provided by the detector. In a trigger system this rate is cut down in basically two steps: the Level-1 (L1) Trigger [24] and the High-Level Trigger (HLT) [25]. The first is a hardware system and contains programmable electronics that reduce the flush of data to a rate of about 30 kHz (design output rate is 100 kHz, but a safety factor of three is assumed). The HLT is a software-based trigger and refines the purity of physics objects. On average it selects a rate of 400 Hz for offline storage [26].

Event and physics object reconstruction The detector incorporates many components whose data must be combined to reconstruct physics objects, i. e. particles and their properties. The so-called Particle Flow (PF) Algorithm [27] has been developed for this purpose. It uses information from all detector parts to identify and reconstruct particles. Electrons and photons are identified based on the track and the energy deposit in the ECAL. Neutrinos are very unlikely to be detected due to their small interaction probability which is why most of them leave the detector undetected. But given the fact that the initial transverse momentum is zero in good approximation, one can firstly sum up the vectorial momenta of the reconstructed particles and secondly take the negative value of that as the missing transverse momentum,

$$\vec{p}_T^{\,\text{miss}} = -\sum \vec{p}_T \,.$$

For this the PF algorithm is used. It shifts the $\vec{p}_T^{\,\text{miss}}$ according to the jet energy correction (JEC) [28, 29] by comparing the uncorrected and corrected jet energies in each event.

Electron reconstruction can have a different behaviour in actual collision data and simulated samples (Section 4.2.1). In order to be still able to compare these two, one can derive so-called scale factors addressing the differences in reconstruction efficiency between data and simulation. The latest 2017 factors are provided by the E/gamma POG [30] and applied to the simulation samples.

4. Used Samples

4.1. Data samples

This analysis is performed on the full 2017 dataset displaying 41.5 fb^{-1} of integrated luminosity. It only operates on certified runs[1]. The SingleElectron and SinglePhoton samples of each run are used (see also Section 5.3) in their latest version of reconstruction from 31st March 2018. The specific run information and the luminosities can be found in Table 4.1.

Table 4.1.: Overview of the used data samples within the analysis. Information on the golden run ranges, the integrated luminosity and the dataset name is provided. Based on [32].

Run	Run Range	Integrated Luminosity $\mathcal{L}/\mathrm{fb}^{-1}$	Dataset Name
Run B	297047-299329	4.79	Data_Run2017B-31Mar2018-v1
Run C	299368-302029	9.63	Data_Run2017C-31Mar2018-v1
Run D	302030-302663	4.25	Data_Run2017D-31Mar2018-v1
Run E	303818-304797	9.31	Data_Run2017E-31Mar2018-v1
Run F	305040-306460	13.54	Data_Run2017F-31Mar2018-v1

The dataset paths are

- */SingleElectron/Run2017*R*-31Mar2018-v1/MINIAOD* and
- */SinglePhoton/Run2017*R*-31Mar2018-v1/MINIAOD*,

where R stands for the run (R $\in \{B, C, D, E, F\}$).

Data hierarchy The CMS data is arranged into data tiers. Each tier contains each physics event but different tiers contain a different amount of information for each event. The first tier is the RAW format which contains full event information and "raw" detector information. The RECO tier samples already include reconstructed physics objects but due to its extent, it is barely used for analyses. The last tier is the AOD which stands for "Analysis Object Data" and is a filtered version of the RECO event information. The samples are further stripped by a small amount of information that is not essential for most analyses [33], yielding the miniAOD samples used in this analysis.

[1] These runs are specified in [31] in the EOY2017ReReco_Collisions17_JSON file.

4.2. Simulated samples

In order to be able to perform an analysis of event data with the purpose of finding possible deviations to the Standard Model expectation one needs information to compare the measured data with. This information is given by simulated (Monte Carlo, MC) samples that represent the expected SM behaviour.

The simulated samples are available either on generator (gen) or on reconstruction (reco) level. On gen level, the information is equivalent to the actual simulated particle properties. On reco level, the samples have been processed in detector simulation software. This virtual detector – a complete replication of the CMS detector – detects the gen particles. This detection process is, like in the real detector, related to uncertainties and small deviations. Thus, the reco and gen level information can differ.

There are several generators of MC samples. Pythia 8.2 [34], MadGraph5 [35] and PowHeg [36, 37] are the most common ones. Different generators produce samples at different perturbation orders of the corresponding cross section: leading order (LO), next-to-leading order (NLO) or next-to-next-to-leading order (NNLO). The samples are generated with different numbers of events. In order to make the samples comparable to each other and to the data they are normalized to an integrated luminosity of $1\,\mathrm{pb}^{-1}$ and a cross section of 1 pb. In a second step, the MC samples are weighted by a factor of

$$w = \frac{\sigma \cdot \mathcal{L}}{N_{\mathrm{MC}}},$$

where σ is the full cross section for the process, $\mathcal{L}$ the integrated luminosity of the used collision data and N_{MC} the number of simulated events in the MC sample. This ensures a correct matching in integrated luminosity between the MC samples and the used dataset. In addition, a so-called "k-factor", a cross section correction factor, is applied to some MC samples.

$$k = \frac{\sigma_{\mathrm{(N)NLO}}}{\sigma_{\mathrm{LO}}}, \quad \text{i.e. for the W samples: } k(M_{\mathsf{W}}) = \frac{\sigma_{\mathrm{(N)NLO}}(M_{\mathsf{W}})}{\sigma_{\mathrm{LO}}(M_{\mathsf{W}})}$$

This factor corrects the cross section used in LO simulation to the one known from theoretical cross section studies at higher orders [38]. This can be done either with a flat factor that is constant for every sample of a process or in dependence of a certain property, for example the mass of the produced W boson.

The MC samples for some processes are binned into certain H_T intervals. The variable H_T is the transverse hadronic energy, denoting the sum of the transverse momenta of all non-leptonic particles on generator level. For any binned sample, region overlaps have been removed to avoid double-counting of events.

4.2.1. Background prediction

An overview of the used background samples is included in the following list:

- off-shell W boson: The dominant background is the SM W boson via the mode $\mathsf{W} \to l\nu$, where $l = e, \mu, \tau$. It is hard to reduce because it has the same signature compared to the SSM W'. The samples are generated in Pythia 8.2 with the CP5 tune at LO. They are mass-binned and ranging from $M(\mathsf{W}) = 100\,\mathrm{GeV}$ up to 6000 GeV. An additional W mass dependent k-factor is applied.

- W + jets $\rightarrow l\nu$: The W + jets $\rightarrow l\nu$ samples are produced using MadGraph5 with the CUETP8M1 tune at LO. For $H_T > 100\,\text{GeV}$, binned samples from $H_T = 100\,\text{GeV}$ to ∞ are used. A flat k-factor of 1.2138 on the LO cross section is applied.
- $t\bar{t}$, single t: The most dominating process below the W background is the decay of the top quarks, either from $t\bar{t}$ or from single t. The samples are generated with PowHeg [39–41], except the single top s-channel sample which is made with MadGraph5_aMC@NLO [42].
- QCD: The quantum chromodynamics (QCD) background covers jets that are misidentified as electrons. This is possible [43] and also likely due to high cross sections for QCD events. The QCD samples are p_T binned and generated in Pythia 8.2.
- Drell-Yan ($\mathsf{Z}/\gamma \rightarrow ll$): Due to some leptons being out of the acceptance region of the detector or to not identified leptons, the final state ll may be registered as $l + \vec{p}_T^{\,\text{miss}}$. This can, for instance, come from so-called Drell-Yan processes where a Z boson or a photon (γ) decays to two charged leptons. The $Z \rightarrow ee$ samples are generated at next-to-leading order (NLO) with PowHeg and mass-binned from 50 GeV to ∞. The γ decay is simulated at LO with MadGraph5. The simulation is H_T binned from 40 GeV to ∞
- Diboson (WW, WZ, ZZ): The Diboson process $pp \rightarrow WWX$ or WZX or ZZX can lead to a $e + \vec{p}_T^{\,\text{miss}}$ final state if the produced bosons decay leptonically (two charged leptons or, for the Z boson, two neutrinos) and jets. The corresponding MC samples are produced with PowHeg, Pythia 8.2 and MadGraph5_aMC@NLO. One triboson sample (WZZ) is generated, too. It is made with Pythia 8.2.

A detailed table containing all background samples with their corresponding cross sections can be found in the appendix in Table A.1. The samples are used in their 2016 version.

4.2.2. Signal samples

In order to compare the collision data and SM background to potential new physics, signal samples for the $\mathsf{W}' \rightarrow e\nu$ process have been produced. The generator is Pythia 8.2 with Tune CUETP8M1, working at leading order and using the CTEQ6.L1 parton distribution functions (PDFs). Higher order corrections (NNLO) are taken into account via a mass dependent k-factor which is calculated using FEWZ [44, 45]. In the appendix, Table A.2 contains an overview of the cross sections in the $e\nu$ decay channel for the generated W' samples.

For the $e + \vec{p}_T^{\,\text{miss}}$ final state, event distributions of different quantities can be used to discriminate between the SM background and the signal that is searched for. The transverse mass M_T (Equation 3.1) has turned out to have the clearest signature with a Jacobian peak at the tail of the distribution. The leptonic decay of the W' boson is a simple two-body decay. Therefore, in the laboratory frame, one expects a back-to-back lepton-neutrino pair with equally distributed p_T. The M_T distributions for three different W' samples can be seen in Figure 4.1. The Jacobian peak is located at the generated mass of the W' boson. Increasing W' masses lead to a rising off-shell production at lower masses. This is due to the finite amount of energy available from

the collision; this energy splits up to the three individual quarks in each proton so that each quark carries on average about 4.3 TeV along. As a consequence, the production of W′ bosons above that value is increasingly suppressed.

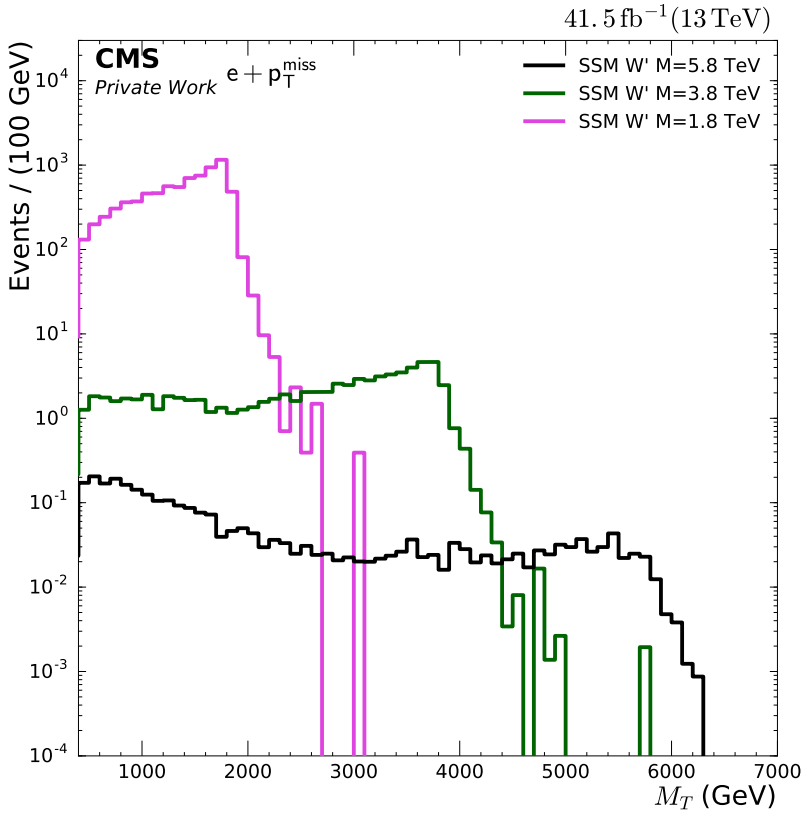

Figure 4.1.: Transverse mass distribution for the W′ → $e\nu$ samples for W′ samples of 1.8, 3.8, and 3.8 TeV. One can see the increasing offshell production for higher W′ masses.

5. General Selection

In this chapter, the general criteria for event selection are presented. It deals with object identification and filtering. Finally, the preceding triggers are described.

5.1. MET/p_T^{miss} filters

In this analysis especially regions of high M_T will be important. In this sector events with high p_T^{miss} values are needed and thus of enhanced interest. But a high p_T^{miss} does not always imply the production of high energy invisible particles, such as the neutrinos in the leptonic W' decay. In fact, issues with detector electronics (predominantly noise), cosmic rays and beam-halo particles can also lead to a high p_T^{miss} (*false* MET, *fake* MET). But since these effects do not originate in the collisions, they need to be excluded as well as possible by using so-called MET filters [46, 47]. The denotation "MET" is slightly outbound and meanwhile even "discouraged" [48]. This is due to the fact that energy is not a directional quantity and that it is the momentum that is actually missing (missing transverse momentum). Therefore, it is increasingly replaced by the $\vec{p}_T^{\text{miss}}$ term. Besides that, the MET filters kept their name until now.

The MET filters applied in this analysis are listed below:

- **HBHE noise filter:** The HCAL contains multichannel hybrid photodiodes (HPDs, Section 3.2.1). They are used to read-out the optical signals from the HB and HE scintillator tiles. The HBHE is known to sporadically record noise signals at a fixed rate that is not dependent on the beam conditions. The noise can be recorded only in one or a few HPD pixels (Ion Noise Feedback Noise), in most or all pixels in one HPD (HPD Noise), or even in nearly all 72 channels in one read-out box (RBX Noise). The HBHE noise filter discriminates mainly via the affected number of occupied HPD pixels [49].
- **HBHE noise iso filter:** Additionally, as an extension to the previously described HBHE noise filter, the isolation-based noise filter uses candidate noise clusters in the HCAL and includes neighbouring activity in ECAL, HCAL, and the tracker into the rejection decision [49].
- **Primary vertex filter:** Events were observed having a lack of tracks compared to the calorimeter deposits. Either the tracking algorithm does not find as many trajectories as there are locations with energy deposits or the collision did not take place in the detector's centre [46]. The filter rejects events fulfilling this characteristic.
- **ECAL dead cell TP filter:** The ECAL has single noisy crystals masked in the reconstruction. In addition, some crystals corresponding to the front end have no data link. As a consequence, some energy deposits may not be recorded and misinterpreted into the $\vec{p}_T^{\text{miss}}$ counting. The filter rejects events where the trigger primitive (TP) E_T of the masked cells saturates at 63.75 GeV [50].

- **Bad PF muon filter:** Events with a not sufficiently reconstructed muon are rejected as that can propagate onto the induced missing transverse momentum. This affects especially muons where the PF and RECO p_T^{μ} differ by 100 GeV [46, 51].
- **Bad charged hadron filter:** Muons of low quality are eventually not declared as PF muons. In this case, this muon makes it into the $\vec{p}_T^{\,\text{miss}}$ calculation of the PF as a charged hadron candidate. The filter excludes these events [51].
- **Beam halo filter:** Particles can be produced through beam-gas or beam-pipe interactions. These particles form the so-called halo. They can interact with the calorimeters and cause energy deposits manipulating the $\vec{p}_T^{\,\text{miss}}$ [52]. They are filtered out by the beam halo filter.
- **Bad EE Supercrystal filter:** In 2012, two crystal regions in the ECAL were found giving anomalously high energies. This is due to high amplitude anomalous pulses, measured in several channels at once and probably coming from high voltage issues. This filter rejects events with such a signature in the p_T^{miss} [48].

Following the recommendations [47], all filters are used both for the collision data and the simulated MC samples. Only the Bad EE Supercrystal filter is not applied to Monte Carlo, as this is not suggested to do.

5.2. Electron identification

In order to identify particles correctly as electrons the electron identification criteria for high p_T are used (High Energy Electron Positron, or HEEP short). This HEEP ID is used in its latest version 7 [53] and its selection criteria are displayed in Table 5.1.

Table 5.1.: HEEP ID v7.0 selection criteria. Taken from [53].

variable or criterion	barrel condition	endcap condition
E_T	$> 35\,\text{GeV}$	$> 35\,\text{GeV}$
η range	$\eta_{\text{SC}} < 1.4442$	$1.566 < \eta_{\text{SC}} < 2.5$
isEcalDriven	$= 1$	$= 1$
$\Delta\eta_{\text{in}}^{\text{seed}}$	< 0.004	< 0.006
$\Delta\phi_{\text{in}}$	< 0.06	< 0.06
H/E	$< 1\,\text{GeV}/E + 0.05$	$< 5\,\text{GeV}/E + 0.05$
full 5x5 $\sigma_{i\eta i\eta}$	n/a	< 0.03
full 5x5 $E^{2\times5}/E^{5\times5}$	> 0.94 or $E^{1\times5}/E^{5\times5} > 0.83$	n/a
EM + Had Depth 1 Isolation	$< 2 + 0.03E_T + 0.28\rho$	$< 2.5 + 0.28\rho$ for $E_T < 50$ else $< 2.5 + 0.03\,(E_T - 50) + 0.28\rho$
Track Isol: Trk Pt	< 5	< 5
Inner Layer Lost Hits	≤ 1	≤ 1
d_{xy}	$< 0.02\,\text{mm}$	$< 0.05\,\text{mm}$

The variables mostly consist of detection geometry and isolation criteria. They are briefly explained in the following listing [54]. The stretch of cones around a certain track is measured in radii of ΔR, e. g. a cone of radius 0.3 includes all points as near as a $\Delta R \leq 0.3$ difference to the track.

- $\boldsymbol{E_T}$**:** The corrected energy deposit in the ECAl times $\sin\theta$, where θ is the polar angle of the electron measured at the very inner layer of the tracker.
- $\boldsymbol{\eta_{SC}}$**:** The supercluster's (SC) pseudorapidity where the electron was measured. A supercluster is a cluster of crystals in the ECAL.
- **isEcalDriven:** This ensures the electron to be found by the ECAL. Besides, the reconstruction via the PF algorithm is still possible.
- $\boldsymbol{\Delta\eta_{in}^{seed}}$ **and** $\boldsymbol{\Delta\phi_{in}}$**:** The difference in η and ϕ, respectively, between the electrons trajectory in the inner tracker and the supercluster in the ECAL.
- $\boldsymbol{H/E}$**:** The ratio between the hadronic energy H deposited in a cone of radius 0.15 around the electrons track and the energy deposit E of the electron in the ECAL's superclusters.
- **full 5x5** $\boldsymbol{\sigma_{i\eta i\eta}}$ **and full 5x5** $\boldsymbol{E^{2\times5}/E^{5\times5}}$**:** The spread in η in units of crystals in a 5×5 crystal cluster around the centre (seed) crystal. $E^{2\times5}$ and $E^{5\times5}$ denote the energy deposit in the ECAL in an array of 2×5 and 5×5 crystals around the seed crystal.
- **EM + Had Depth 1 Isolation:** The transverse energy of all reconstructed hits in the ECAL with $E > 0.08\,\text{GeV}$ within a cone of radius 0.3 centred on the electron's position in the ECAL. The Had Depth 1 denotes the HCAL energy depositions in a cone of radius 0.3 excluding an inner core of radius 0.15. These two energies are added and compared to the E_T of the electron and the mean energy density per unit area ρ. This is supposed to suppress jets misidentified as electrons.
- **Track Isol: Trk Pt:** The sum of all p_T within a cone of radius 0.3 excluding an inner cone of radius 0.04. It must be smaller than 5 GeV in order to suppress jets as well.
- **Inner Layer Lost Hits:** The number of tracker sensors that did not fire in the reconstructed trajectory. This number must be at most 1 in order to suppress electrons originating from pair production.
- $\boldsymbol{d_{xy}}$**:** The distance between the trajectory and the reconstructed primary vertex.

5.3. Triggers

This analysis uses the single electron trigger as the predominant trigger. Its threshold is 115 GeV and it is applied to data samples as well as Monte Carlo. As investigated in previous analyses [55], the trigger exhibits a sharp turn-on and reaches its fully efficient trigger plateau at 130 GeV. In addition, in order not to suffer an efficiency loss for high p_T electrons as it has been observed earlier, a single photon trigger with a threshold of 200 GeV is added. A trigger efficiency study has been performed by YuChul Yang[1], finding a decreasing single electron trigger efficiency for increasing electron E_T (see Figure 5.1). Adding the single photon trigger as an OR opportunity recovers most of the efficiency loss in that region.

The efficiencies were calculated using the tag-and-probe method. This approach uses a so-called orthogonal muon dataset. The number of events where the muon trigger has fired and an electron has also been produced is compared to the number

[1]Kyungpook National University

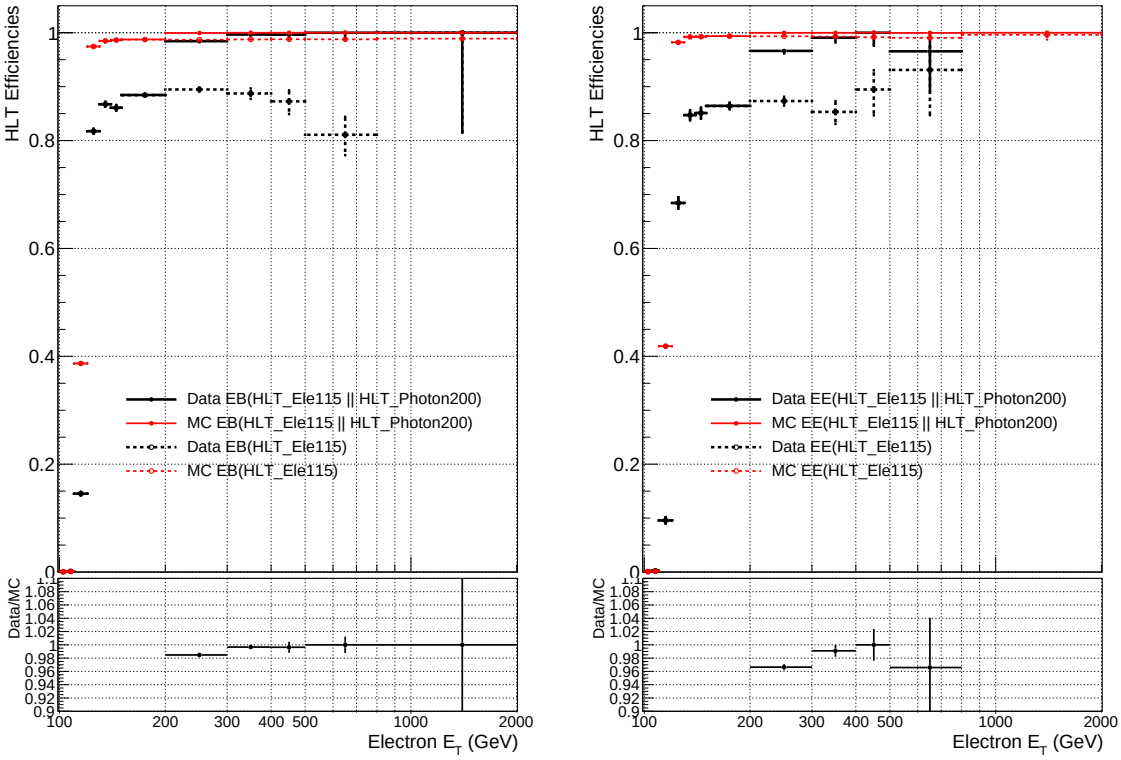

(a) For events in the barrel (EB). (b) For events in the endcap (EE).

Figure 5.1.: Single electron trigger efficiency and efficiency of the combination of the single electron and single photon trigger in the barrel (left) and endcap (right) for data and Monte Carlo. Provided by YuChul Yang.

of events where the muon trigger has fired, an electron has been produced *and* the single electron trigger has fired. The same proceeding is done for the combination of the single electron and single photon trigger. Comparing the efficiencies derived this way for data (ϵ_{data}) and MC (ϵ_{MC}), one can derive so-called trigger scale factors

$$\mathsf{SF}_{\text{trigger}} = \frac{\epsilon_{\text{data}}}{\epsilon_{\text{MC}}}$$

and apply these to the Monte Carlo. This strategy ensures a comparable trigger acceptance behaviour for data and Monte Carlo simulation. All trigger scale factors applied in this analysis can be found in the appendix in Table A.3.

As two datasets containing the single electron trigger are used, a cleaning of the datasets was done in order not to double count equal events. If either the single electron or both triggers have fired, the single electron dataset is used. Instead, the single photon dataset is used if only the single photon trigger has fired.

6. Analysis

6.1. Framework

As described in Section 4.1 this analysis uses miniAOD data samples. They are provided by the CMS Collaboration within the CMS software [56], or CMSSW for short. These already stripped samples typically still contain information that is redundant for most analyses. For this reason, the miniAODs are further processed by software tools originating in the Physics Institute IIIa in Aachen, called "Three A Physics Analysis Software" (or short, TAPAS) [57]. The samples are skimmed within this software and the output is stored in the file format "pxlio", generated by the PXL library [58]. These files are used as the input data for the analysis.

6.2. Pile-up reweighting

As mentioned in Section 3.2, colliding bunches of many protons leads to many interactions per bunch crossing. Due to these additional total inelastic interactions, each event contains an increased number of primary vertices, which is called pile-up. At CMS, the number of additional pile-up interactions for an event is calculated via a luminosity-based estimate. For each bunch crossing the instantaneous luminosity is measured and then multiplied by the total inelastic cross section, called minimum bias cross section, for *pp* collisions. Finally, the vertex reconstruction efficiency of about 70 % leads to a slight increase in this calculated number of vertices per event [59]. Following the Lumi POG recommendations, the minimum bias cross section is $\sigma = 69.2\,\mathrm{mb}$; it derives from a "best-fit" approach [60].

The pile-up correction factor

$$w_{\text{pile-up}} = \frac{N_{\text{vertices}}^{\text{data}}}{N_{\text{vertices}}^{\text{MC}}}$$

is then used to correct the simulation samples to the specific pile-up conditions. Here, $N_{\text{vertices}}^{\text{MC}}$ is the number of primary vertices in the data and $N_{\text{vertices}}^{\text{MC}}$ is the corresponding number in the MC simulation samples. This calculation process is done individually for events grouped in a section of nearly constant instantaneous luminosity (luminosity section).

In Figure 6.1 one can see the number of primary vertices distribution for the samples described in Chapter 4 before and after applying the pile-up correction to the simulation. The background splits up into different parts as explained in Section 4.2.1 and those fractions are marked in different colours in a stacked histogram. The actual collision data is represented with black dots and statistical error bars. In addition to that, two signal samples (for W' masses of 1.8 TeV and 3.8 TeV) are shown as solid

lines. The ratio of data and Monte Carlo is shown underneath the distribution. This description of the distribution is valid for most of the distribution shown in the following sections.

One can see a slight shift of the simulation to smaller numbers of vertices. This indicates some issues regarding the process of reweighting. A possible cause for this could be a slightly inaccurate value for the minimum bias cross section as this is the main variable affecting the reweighting process.

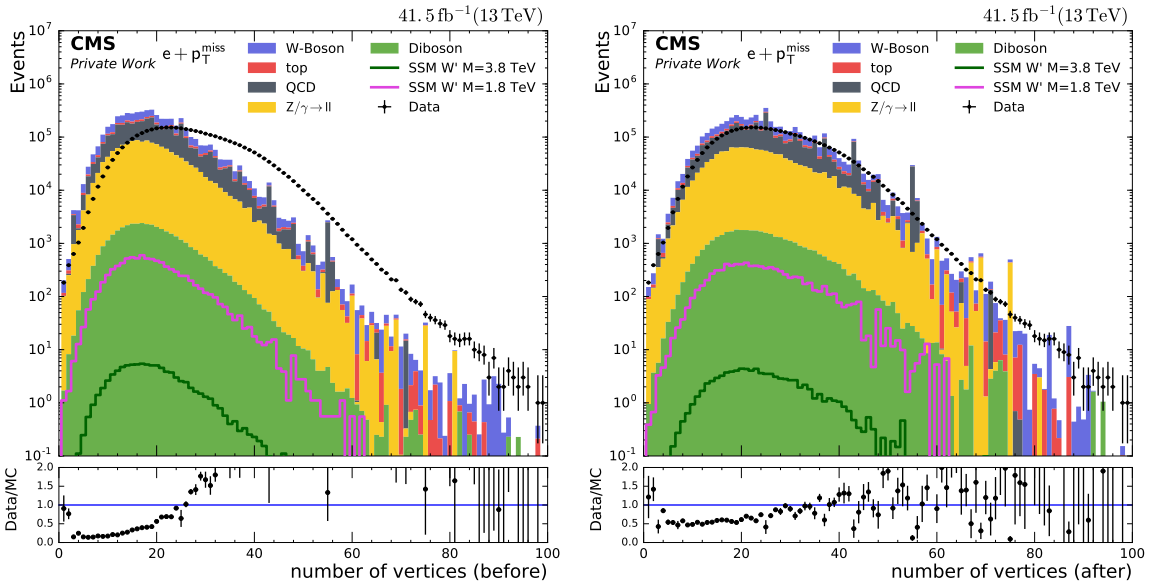

(a) Before the pile-up correction.

(b) After the pile-up correction.

Figure 6.1.: The number of vertices distribution. One can see the approximate and average number of 20 interactions per bunch crossing.

6.3. Selection criteria

The samples listed in Chapter 4 must fulfill the general selection criteria described in Chapter 5. This selection stage is called PreSelection in the following. Only events in accordance with the electron HEEP identification, the MET filters, and passed trigger criteria reach this stage.

In addition to this rather generic selection, further analysis specific selection criteria are applied. Firstly, some quality cuts are made. They include a veto on a second lepton (e, μ, τ) with $p_T > 25\,\text{GeV}$. Furthermore, an electron transverse momentum of $p_T^e > 200\,\text{GeV}$ is demanded in order to harmonise the triggers' event selection of the single electron (threshold 115 GeV) and single photon trigger (200 GeV). The p_T^{miss} is required to be greater than 150 GeV to cut out potentially mismodelled low p_T regions.

In order to take into account the signal's nature, kinematic selection criteria are utilized. As explained in Section 4.2.2, a back-to-back decay of the W′ boson is expected, giving equal momenta fractions to the lepton (electron) and the neutrino. Therefore, cuts requiring the ratio of electron and missing transverse momentum to

fulfill $0.4 < p_T^e/p_T^{\text{miss}} < 1.5$ as well as the azimuthal angle between electron and the $\vec{p}_T^{\text{miss}}$ vector to satisfy $\Delta\phi(e, \vec{p}_T^{\text{miss}}) > 2.5 \approx 0.8\pi$. As one can see in Figure 6.2, the signal contribution is mainly located in these two regions, which is why they are called "signal regions". These requirements have been optimized for and used in earlier $W' \to l\nu$ analyses [1, 3] and are adopted to this thesis.

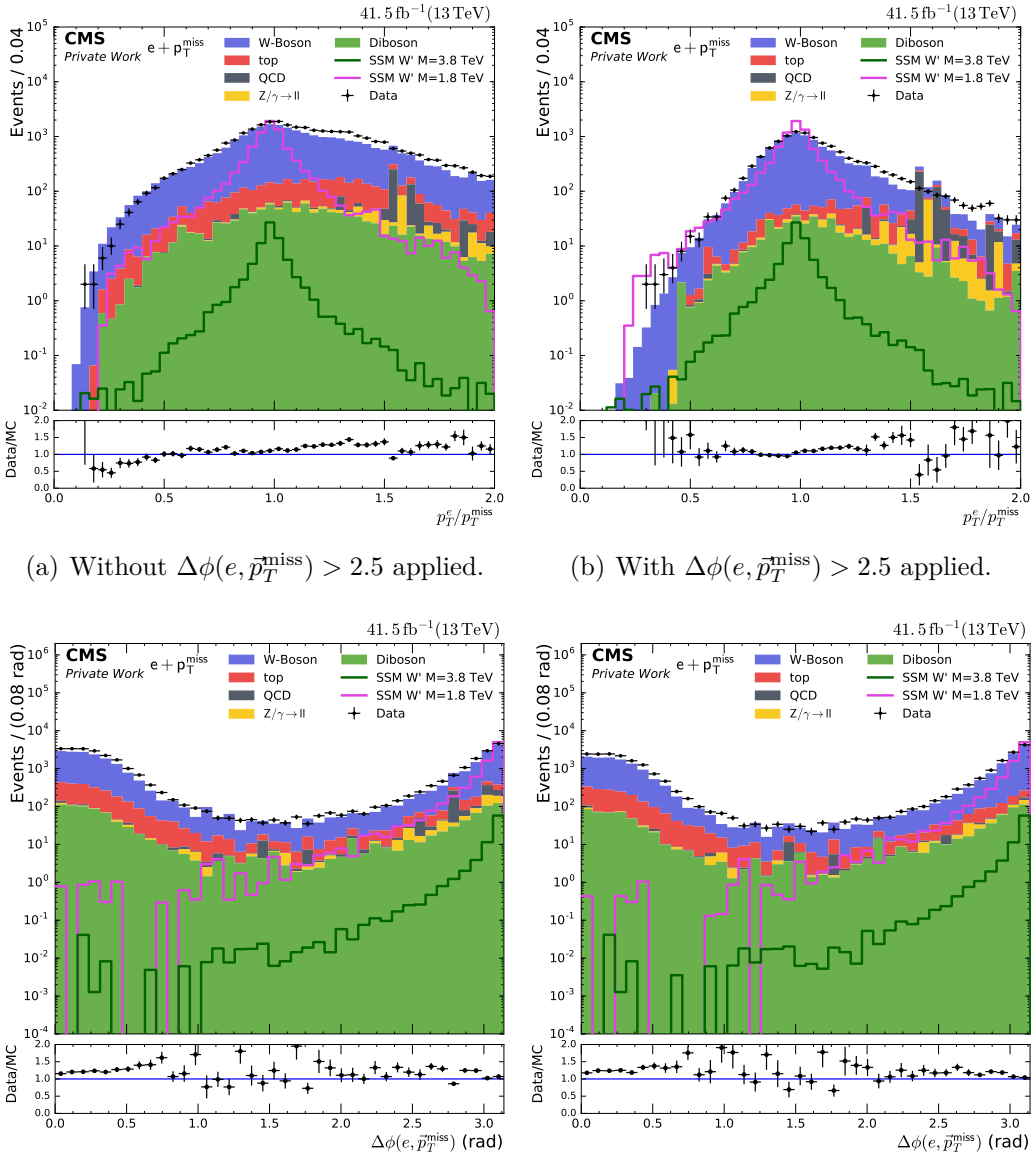

(a) Without $\Delta\phi(e, \vec{p}_T^{\text{miss}}) > 2.5$ applied.

(b) With $\Delta\phi(e, \vec{p}_T^{\text{miss}}) > 2.5$ applied.

(c) Without $0.4 < p_T^e/p_T^{\text{miss}} < 1.5$ applied.

(d) With $0.4 < p_T^e/p_T^{\text{miss}} < 1.5$ applied.

Figure 6.2.: The ratio p_T^e/p_T^{miss} of electron and missing transverse momentum (top) and $\Delta\phi(e, \vec{p}_T^{\text{miss}})$ (bottom) distributions. The left histograms show the distributions without the other kinematic cut, the right ones with it.

6.4. Full Background Prediction

In order to see the impact of each criterion applied to the used samples, Figure 6.3 shows the remaining number of events after each selection requirement. Starting with nearly 10^9 real data events in the sum of all samples, the requiring of the trigger selection, MET filters and HEEP ID in the PreSelection has the biggest impact on the following event yield. It reduces the remaining number down to less than 10^7. Data and Monte Carlo are comparable from the fourth stage (p_T^e cut) on when trigger turn-on effects are excluded due to the electron p_T threshold. A slight surplus in data is observed, it is investigated in Section 6.6.2.

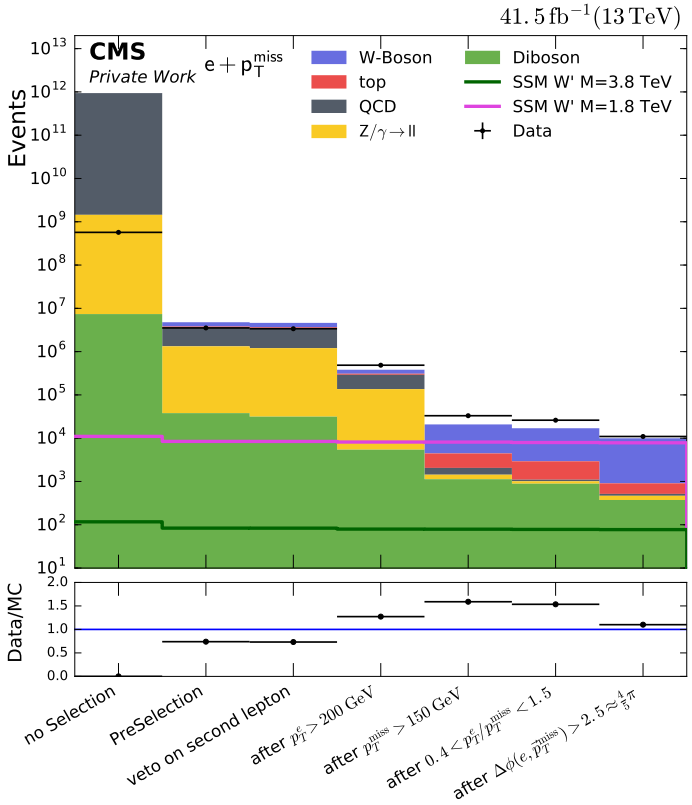

Figure 6.3.: The impact of each selection step visualised by the number of remaining events. The second stage, the PreSelection, includes a fulfilled HEEP ID and trigger thresholds and has MET filters applied.

In the following, the Standard Model background is compared to the measured collision data showing event distributions of geometric and kinematic variables. The distributions are shown on the stage after requiring all selection criteria described before.

In Figure 6.4, the ϕ and η distributions of the electron are shown. These fundamental geometric quantities provide a qualitative comparison between data and MC. The azimuthal angle ϕ is in good approximation uniformly distributed. This is expected, as there is no preferred decay direction in a setup with vanishing total transverse momentum before the collision. In η, one can clearly see the overlap regions of barrel and endcap at $\eta = \pm 1.4$. At these two points, as well as at high positive and negative η one

can see deviations between simulation and data. This indicates problems simulating the barrel-endcap overlap and the very forward and backward regions. Nevertheless, this does not have an effect on this analysis' final distributions since the overlap region is cut out by the HEEP ID (see Table 5.1).

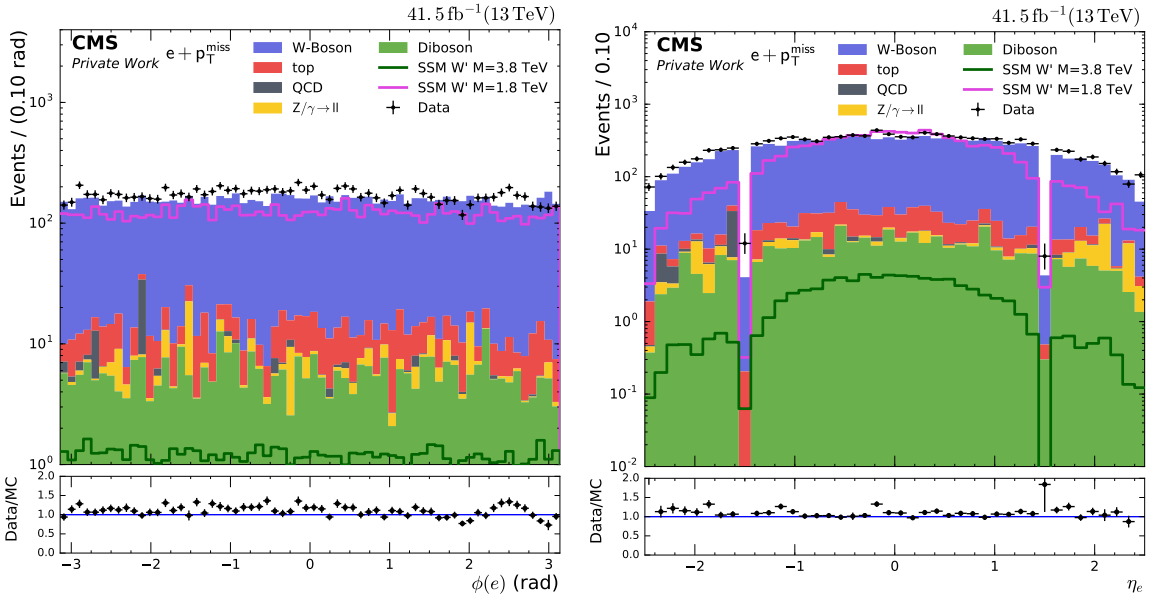

Figure 6.4.: The ϕ (left) and η (right) distributions of the electron. Whilst, the events are uniformly distributed in ϕ, the η distribution is centered around 0. One can see the overlap region of barrel and endcap, leading to issues in the agreement of data and simulation.

As a kinematic quantity, the distributions of the electron p_T and the missing transverse momentum p_T^{miss} are shown in Figure 6.5 and 6.6. Both quantities show a good agreement between data and simulation. A slight decreasing tendency in the data/MC ratio is noticed. The trend reduces after applying the kinematic selection. This is, in particular, due to a significant reduction of the top background by these cuts.

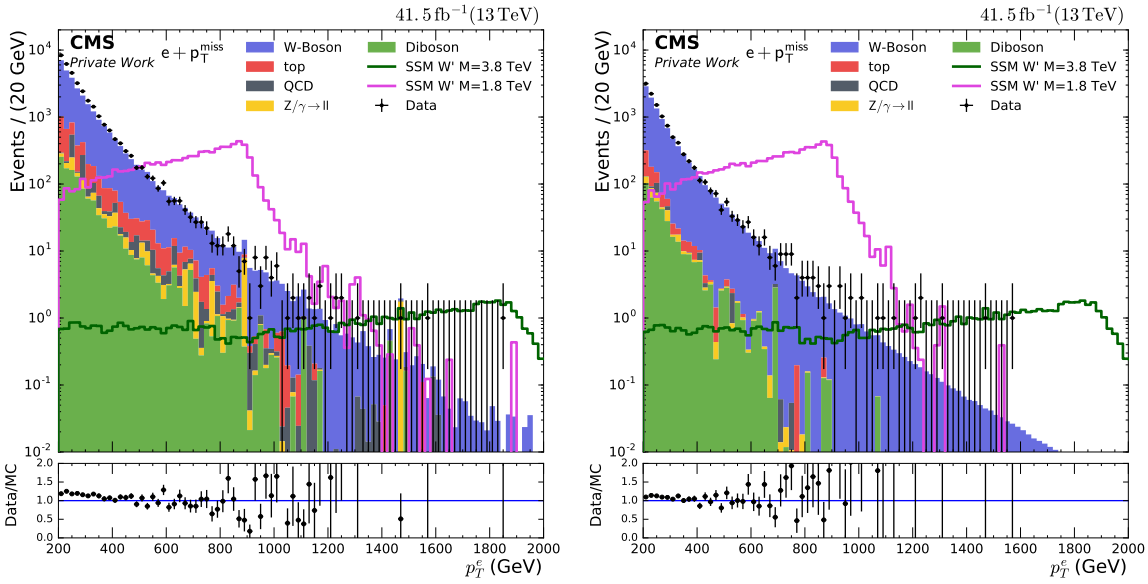

Figure 6.5.: Distribution of the electron p_T before (left) and after (right) applying the kinematic selection criteria. As one can see the signal shape remains nearly untouched, as it is desired. Data and simulation show a good agreement.

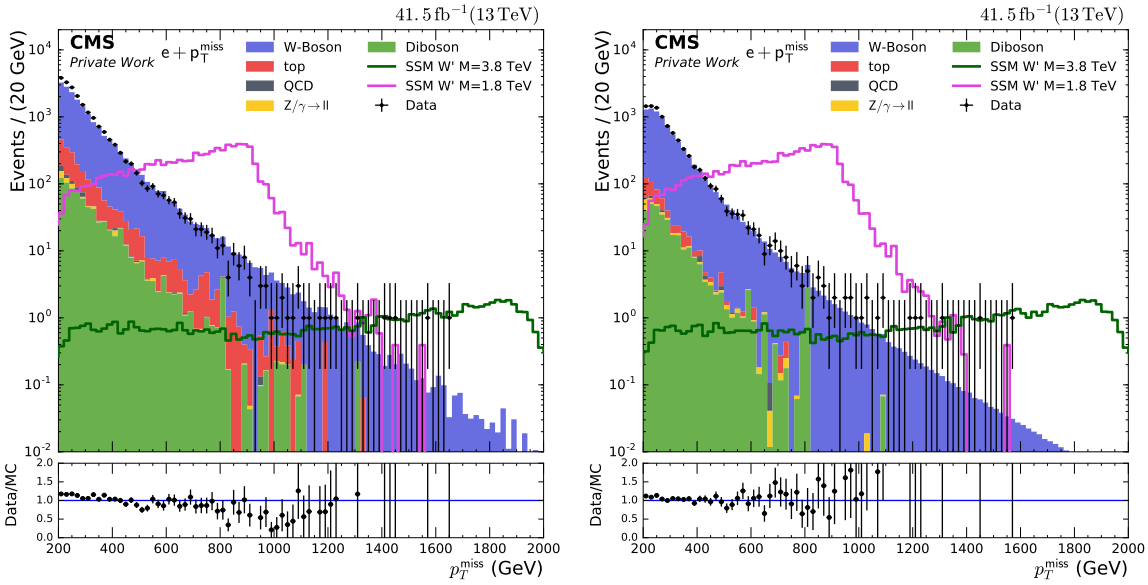

Figure 6.6.: Distribution of the missing transverse momentum p_T^{miss} before (left) and after (right) applying the kinematic selection criteria. As one can see the signal shape remains nearly untouched, as it is desired. Data and simulation show a good agreement.

6.5. Evaluation of systematic uncertainties

Every experiment implicates uncertainties, statistical as well as systematic ones. Concerning particle physics experiments dealing with event numbers, the statistic uncertainties arise from the Poisson error ($\sqrt{N}$, where N is the number of counted events). The systematic uncertainties have different sources and affect either the shape of kinematic distributions or the normalization, as for example for the luminosity uncertainty. They are evaluated by repeating the whole analysis flow with the uncertainty specific values shifted in both ways, following the official recommendations. The uncertainties are furthermore important for the Limit Setting process in Section 6.7.

In the following, all sources of systematic uncertainties are listed:

- **Luminosity:** Following the official recommendations concerning the 2017 luminosity measurement [61], the systematic uncertainty on the luminosity is set to 2.3%.
- **Pile-Up:** Following the LUMI POG recommendations [60] the minimum bias cross section ($\sigma = 69.2\,\text{mb}$, see Section 6.2) has an uncertainty of 4.6%. Again, the impact on the shape of a kinematic distribution is then evaluated by performing the analysis with the cross section shifted by its uncertainty.
- **Electron scale factors:** Reconstruction as well as triggering each use scale factors in order to account for different behaviour in MC and data (see Section 3.2.2 and 5.3). These scale factors bring along systematic uncertainties. The analysis is repeated with scale factors shifted by their uncertainty. The trigger scale factor uncertainty is the dominant one, it starts at less than 1% for low p_T electrons and increases to about 8%.
- **Electron energy scale:** The scaling of the electron energy has a systematic uncertainty that is derived comparing Monte Carlo and data in the region of the Z boson peak. The uncertainty is 0.4% in the barrel and 0.8% in the endcaps.
- **Jet energy scale:** The jet energy has an uncertainty, it is provided by the recommended Jet Energy Correction (JEC) [29]. It depends on the jet p_T and η, the numbers can be found in [62]. Regardless of the fact that jets are not part of the selected final state in this analysis, the energy corrections are important for the calculation of the $\vec{p}_T^{\,\text{miss}}$ uncertainty.
- **Jet energy resolution:** The resolution of the jet energy depends on the jet p_T and η, too. The energy is varied using a Gaussian distribution with the initial energy value as its mean and the resolution as the standard deviation. All jet energy uncertainties affect the uncertainty of the $\vec{p}_T^{\,\text{miss}}$.
- **$\vec{p}_T^{\,\text{miss}}$ scale:** The uncertainty on the missing transverse momentum is calculated by propagating the energy uncertainties of all other objects (e. g. jets, electrons) in the event, since the $\vec{p}_T^{\,\text{miss}}$ vector depends on all these values. The difference of the $\vec{p}_T^{\,\text{miss}}$ to its value calculated with the unshifted values is taken as its uncertainty. Unclustered energy, that has not been connected to a reconstructed physics object, is also used in the $\vec{p}_T^{\,\text{miss}}$ calculation. Its uncertainty is set to 10%.
- **PDF:** The collided particles, protons, are made of quarks and gluons (see Section 2.1.3). Thus, every single one of these partons carries a certain amount of momentum which is described by Parton Distribution Functions (PDFs). In total 100 different PDF sets are used for modelling this, following the recommendation

for LHC Run II of the PDF4LHC group [63]. The differences in these approaches are combined and the change in the background prediction is evaluated bin by bin. This results in an uncertainty on the theoretical cross section which has an effect on the background normalization. This propagation is not done for the signal since the signal cross section is the parameter of interest in limit setting (see Section 6.7).

- ***k*-factor:** There are two different approaches for combining electroweak and QCD cross section corrections, an additive and a factorized, yielding possibly different results for the k-factor. This results in an uncertainty, which was evaluated to be around 5% at most.

6.6. Final distributions

6.6.1. Resolution study

In order to find the optimal bin width for the transverse mass distribution, a study on the resolution in M_T has been performed. In the best case, the bin width of a distribution should be in accordance with the uncertainty of the corresponding quantity. The relative resolution in M_T is estimated by comparing the generated (M_T^{gen}) and reconstructed (M_T^{reco}) transverse mass of each event. For this, only signal events are used in order to achieve a resolution matching to the signal searched for. In a histogram, the quantity

$$R \equiv \frac{M_T^{\text{gen}} - M_T^{\text{reco}}}{M_T^{\text{gen}}}$$

is plotted against the number of number of events for each signal point. As an example, in Figure 6.7, one can see such a distribution for the $M_{\text{gen}}(W') = 5000\,\text{GeV}$ signal sample. In the next step, a fit to each distribution is done using a modified Lorentz function,

$$N(R) = A \cdot \frac{1}{\left[(R-d)^2 - \omega_0^2\right]^2 + \gamma^2\omega_0^2}\,, \tag{6.1}$$

where N is the number of events in dependence of the relative resolution R for each event. The parameters ω_0 and γ define the peak shape of the function curve. A denotes a normalization factor in order to take into account the correct height of the fitted curve and d is a displacement in horizontal direction to center the curve appropriate. The fitting interval of this function is $R \in [-0.06, 0.06]$. It has been restricted to these values because of deviations for higher $|R|$ values. In Figure 6.7 the red line indicates the fitted curve $N(R)$.

One can now define the resolution R_{M_T} as the Full Width Half Maximum (FWHM). For the function in Equation 6.1 it is

$$R_{M_T} \equiv \text{FWHM}\left[N(R)\right] = \left|\sqrt{\omega_0^2 + \gamma\omega_0} - \sqrt{\omega_0^2 - \gamma\omega_0}\right|\,.$$

The resolution's uncertainty is given by the fit errors of ω_0 and γ propagated onto R_{M_T}. The calculated values for each signal masspoint are plotted in Figure 6.8(a). Figure 6.8(b) shows the relative resolution multiplicated with the generated W′ mass

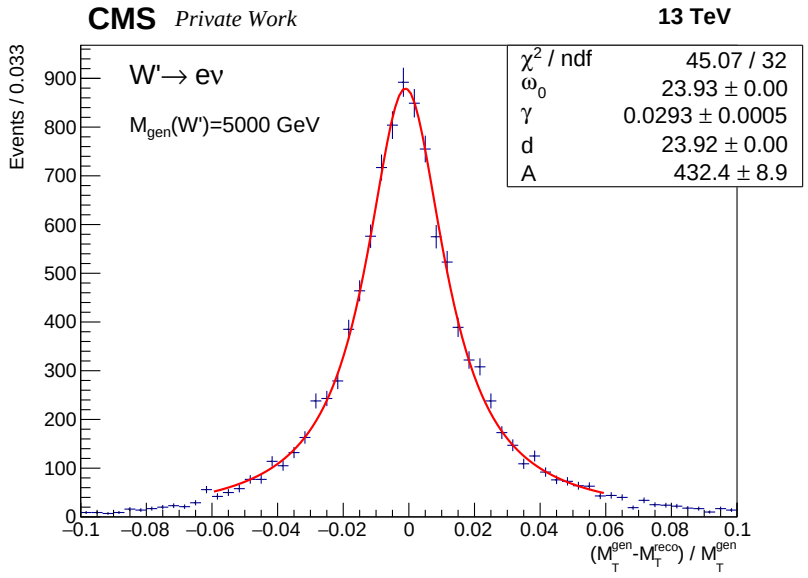

Figure 6.7.: Exemplary resolution histogram for the $M_{\text{gen}}(W') = 5000\,\text{GeV}$ signal sample.

yielding an estimation for the absolute resolution in M_T. The red line indicates a polynomial fit of degree 3 (parameters $p0, p1, p2, p3$ corresponding to the powers of the fitted polynomial). Its purpose is to simplify reading off appropriate resolution values.

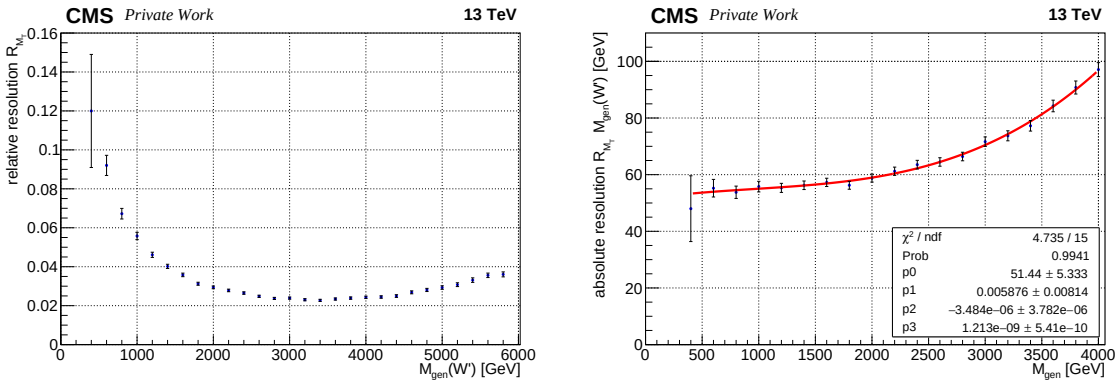

(a) Relative resolution R_{M_T}.

(b) Absolute resolution $R_{M_T} M_{\text{gen}}(\text{W}')$.

Figure 6.8.: Signal resolution in the transverse mass M_T.

Thus, the bin widths have been chosen according to the absolute resolution. One can construct intervals of the same bin width, as it is listed in Table 6.1.

6.6.2. Transverse mass distribution

After applying all selection criteria described in the previous sections and setting adequate bin widths, the final distribution of the discriminating variable M_T is shown in Figure 6.9. Additionally, a cumulative distribution is shown that, for each bin, indicates the number of events with a transverse mass higher than that specific M_T value. In

Table 6.1.: Found optimal bin widths for the transverse mass distribution.

M_T interval [GeV]	bin width [GeV]
300-1980	60
1980-2820	70
2820-3380	80
3380-3650	90
3650-4050	100

both cases, the grey band surrounding the background's bin entries illustrates the range of the systematic uncertainties. Both data and simulation show a steadily declining shape with the W-Boson being the dominant source of SM background events.

For a wide range in M_T, the distributions show good agreement between data and background within the statistical and systematical uncertainties. However, above around 1.5 TeV one can see a slight overfluctuation in data compared to the simulation. Performing a significance test (see e. g. [64]) and considering statistic and systematical uncertainties, this region shows a local significance of 1.70σ. In the regions above 2.0 TeV and 2.5 TeV, one obtaines deviations of 1.43σ and 1.28σ, respectively. The observation can therefore be explained by statistical fluctuations. Despite, the surplus may be due to a lack of statistics since the diboson and top backgrounds vanish almost completely for $M_T > 1.5$ TeV. A background fit could be a possibility to recover background in this region. This would also address the unsteadiness due to low statistics. The latter effect could, of course, also be tackled by new samples including more events.

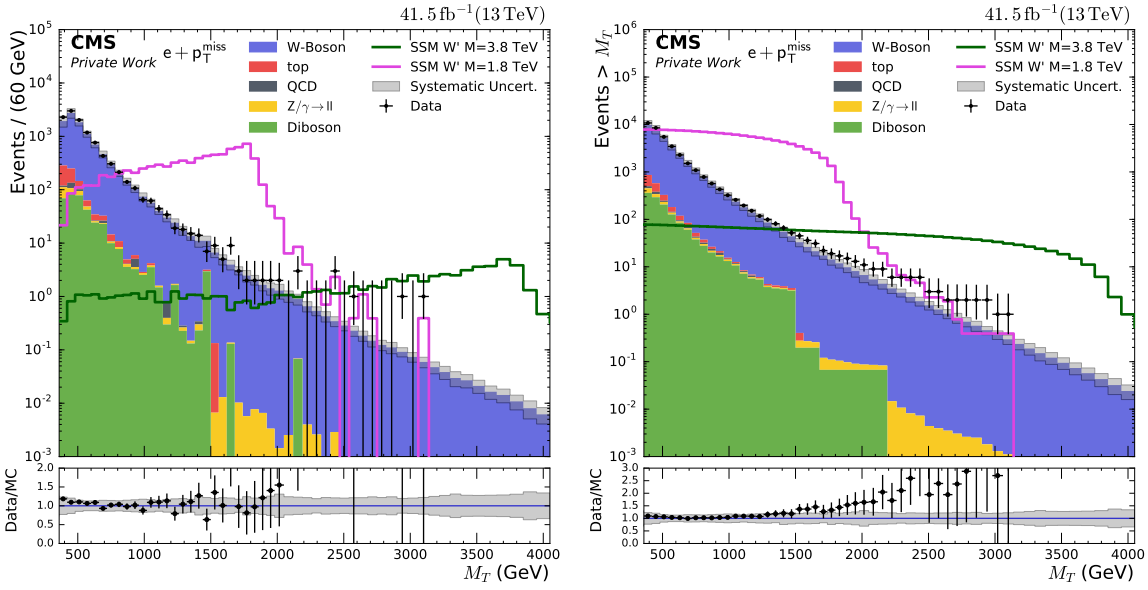

Figure 6.9.: Final distribution of the transverse mass M_T. Shown are the distribution itself (left) and its cumulative version (right). Data and simulation agree for a wide range of masses. Despite the slight overfluctuation in data compared to background prediction in the high M_T region, no significant deviations to the SM have been found.

The highest M_T event contains an electron with a p_T of $1570 \pm 20\,\text{GeV}$ and a p_T^{miss} contribution of $1560 \pm 20\,\text{GeV}$. These two momenta vectors are separated by an azimuthal angle of $3.154 \mathrel{\hat{=}} 180.7°$, showing an almost perfect back-to-back decay signature. In Figure 6.10 an event display of this highest transverse mass event is shown. It has an M_T of $3130 \pm 40\,\text{GeV}$ and was measured in Run F in 2017. It belongs to run 305636 and luminosity section 154 and its event number is 205978044.

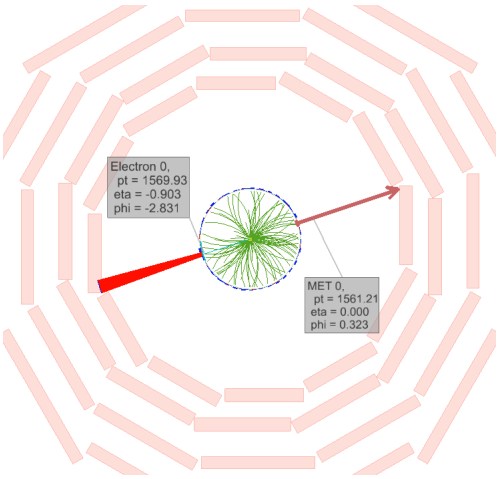

(a) View in the transversal x-y-plane.

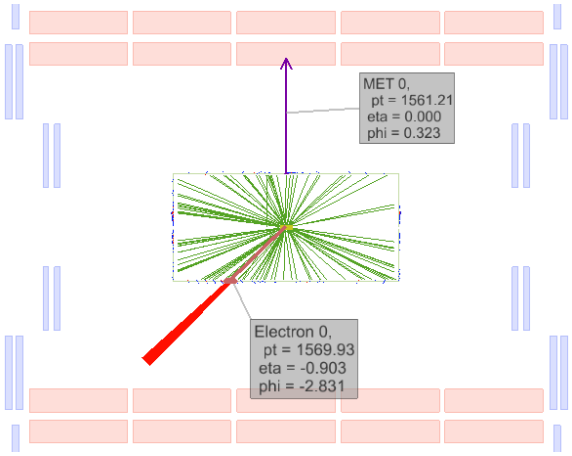

(b) Side view in the y-z-plane.

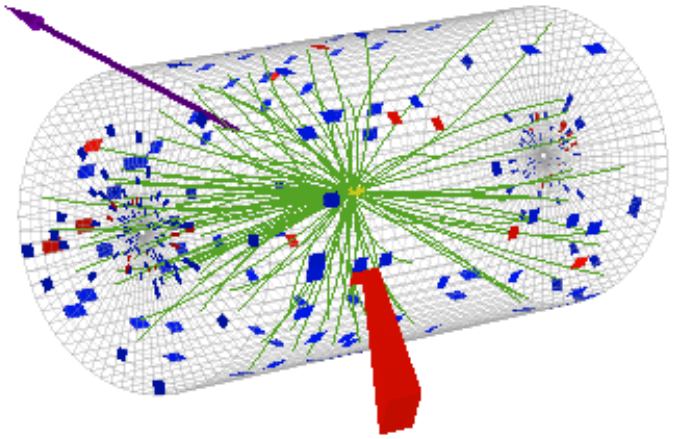

(c) Three dimensional view.

Figure 6.10.: Event display of the highest M_T event of $3130 \pm 40\,\text{GeV}$. Green lines indicates paths reconstructed by the tracker system, the electron's track is highlighted in turquoise. The red cone visualises the energy deposit in the electromagnetic calorimeter and the purple arrow shows the missing transverse momentum vector.

6.7. Statistical Interpretation: Limit Setting

In order to make a substantial statement about physical observations, statistical methods are used. As no significant excess of data compared to the Standard Model expectation has been seen, one can set exclusion limits on parameters of new physics models. In this analysis, the signal cross section is the free parameter a limit can be set on. Doing this for all mass points, one can translate this on the W' mass.

There are different approaches to calculate a limit, such as the modified frequentist method CLs [65] or the Bayesian approach. Whilst the first comes out with a confidence interval that shall include the true value of the parameter of interest, the latter only makes a statement on the probability of the parameter of interest. Both ATLAS and CMS agreed on using the Bayesian approach in W' analyses. It is explained deeper in the following section and used for the limit setting on the W' mass in this analysis.

6.7.1. Bayesian approach

In the notion of Bayesian statistics, probability is associated with the value of a certain parameter. The Bayesian probability for a certain statistical event A – assuming that B is true – is related to the probability of the event B given that A is true,

$$P(A|B) = \frac{P(B|A)P(A)}{P(B)}\,. \tag{6.2}$$

In the context of an experiment, the value of the parameter to be determined, say θ, is based on a vector of data $\vec{x}$. Using Bayes' theorem 6.2, this yields

$$p(\theta|\vec{x}) = \frac{P(\vec{x}|\theta)\pi(\theta)}{P(\vec{x})}\,,$$

where $P(\vec{x}|\theta)$ is the probability density function for the data obtained in the experiment viewed as a function of the parameter θ, often called the likelihood function. $\pi(\theta)$ represents the prior degree of belief into the value θ. Additionally,

$$P(\vec{x}) = \int P(\vec{x}|\theta')\pi(\theta')\,\mathrm{d}\theta'$$

gives the overall probability to observe exactly this set $\vec{x}$ of data. It is obtained by integrating over all possible values of θ, weighted with each value's probability $\pi(\theta)$. This term serves as a normalization factor to the posterior probability $p(\theta|\vec{x})$. By convention, most limits are given at a 95% confidence level (CL). The limit on the model parameter θ can then be yielded by

$$0.95 = \int_0^{\theta_{0.95}} L'(\vec{x}|\theta)\pi(\theta)\,,$$

if 0 is the lowest possible value θ can adopt. In this equation, L' denotes the likelihood, e. g. a Poisson distribution, substituting the probability for the observation of the data vector $\vec{x}$. The likelihood L' takes into account the impact of systematic uncertainties induced by further nuisance parameters $\vec{v}$ by integrating over them,

$$L'(\vec{x}|\theta) = \int L_{\mathrm{Poisson}}(\vec{x}|\theta,\vec{v})\pi(\vec{v})\,\mathrm{d}\vec{v}\,. \tag{6.3}$$

Again, as a weight, $\pi(\vec{v})$ expresses the probability for certain nuisance values $\vec{v}$. L_{Poisson} can be obtained as a Poisson distribution characterized by the number of counted signal events n and the expected number of events from background and signal $\epsilon(\theta, \vec{v})$, being a function of the model parameter θ and the possible further nuisance parameters $\vec{v}$. For reference, see for example [8] and [17].

Using this method, the calculation of the limits was perfomed by the "Higgs Combine Tool" [66, 67], a framework based on the "RooStats" statistics package [68].

6.7.2. Limits for SSM interpretation

A multi-bin approach for the exclusion limit setting is used in order to take into account the shape information from the M_T distribution. For this purpose, the likelihood function as defined in Equation 6.3 is evaluated in each bin, leading to the combination of all bins in the end.

Figure 6.11 shows the final exclusion limit plot for the cross section times branching fraction of $\mathsf{W}' \to e\nu$ process as a function of the W' mass. The dashed black line indicates the curve shape for the expected limits, only based on the simulation. This line is surrounded by the ± 1 and ± 2 standard deviations bands in green and yellow, respectively. The bold solid black line indicates the observed limit line, taking into account the data points remaining in the final M_T distribution. This line is compared to the theoretical cross section (black line with a grey band). The systematical band visualises the PDF uncertainty on the signals. To set the actual exclusion limit, one has to evaluate the intersection point of the observed curve and the theoretical cross section. At masses higher than at this point, the signal cross section is such small that one must have seen significant excess in data compared to background prediction. Smaller masses can be excluded on a 95% confidence level. The 2017 exclusion limit is evaluated to

$$M(\mathsf{W}') \leq 4.85\,\text{TeV}\,,$$

yielding a slightly smaller value compared to the corresponding 2016 analysis in which the limit was set to 4.9 TeV [4]. This can be explained by the slight surplus in data at the high M_T region, marginally lifting the observed curve and yielding a sooner intersection.

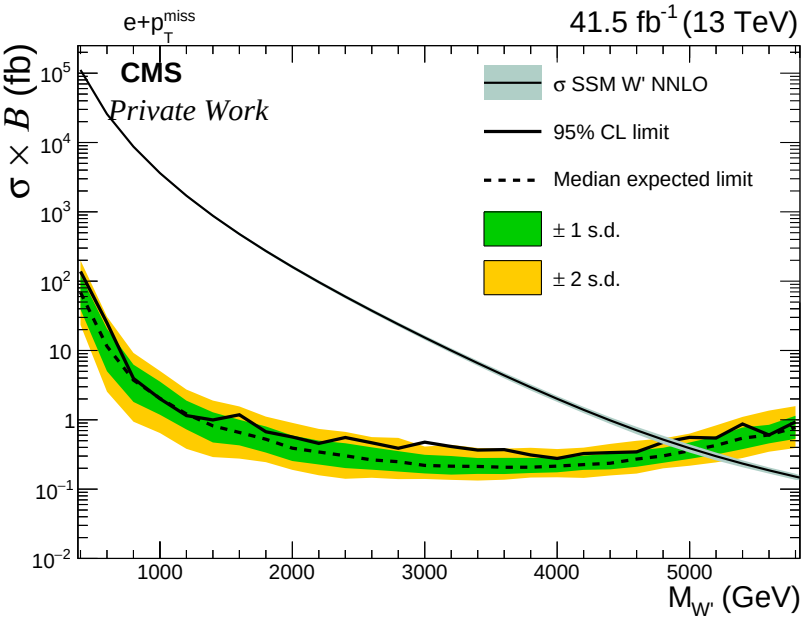

Figure 6.11.: Exclusion limit for the cross section times branching fraction. The limit parameter is the W′ mass. The theoretical cross section is shown with a thick, black line surrounded by its uncertainties (grey). The observed and expected limit are plotted in solid and dashed lines, respectively, and lay within the ±2 standard deviations bands.

7. Vector Boson Fusion processes

In the past few years, some studies have been conducted investigating Vector Boson Fusion (VBF) processes. One focus is laid onto Higgs or Multi-Higgs production, like in [69], whilst other searches deal with potential new heavy vector bosons produced in VBF processes, like a neutral TeV scale Z' boson [70]. The searches have in common to evaluate effects at higher centre-of-mass energies for the collisions carried out. As more beam energy is available, Vector Boson Fusion processes with high mass bosons become more likely. In addition, higher boson couplings to other bosons compared to the boson-quark coupling are possible. The latter has been an object of interest in the Sequential Standard Model searches.

This chapter gives an overview of possible W' searches in VBF processes. For this purpose, signal samples including W' production via VBF processes and its decay to $e + \nu$ are analyzed. Qualitative observations in kinematic distributions are compared to the findings in the SSM W' search.

7.1. Theoretical Background

The ATLAS and CMS physics program includes different approaches to search for new heavy gauge bosons. Looking at it the other way around, VBF related events show high suitability for various searches, such as for dark matter [71] and electroweak supersymmetry [72].

This analysis part focusses on the production of a new heavy charged vector boson through Vector Boson Fusion channels. To distinguish between the SSM W' boson and the new boson in the VBF search, the latter is subsequently denoted with VC, where V is referring to "vector" and C to "charged". The different naming does particularly not imply a different boson nature. One possible Feynman graph of such a VBF process is shown in Figure 7.1. The merging bosons can be replaced by other bosons, such as W and Z, taking into consideration the conservation of all quantum numbers at the fusion vertex.

The VBF topology is characterized by two high p_T forward jets, strongly separated in pseudorapidity and thus located in opposite hemispheres (η positive or negative). The invariant mass m_{j_1,j_2} of the dijet pair is expected on a TeV scale. It is defined as

$$m_{j_1,j_2} = \sqrt{(E_{j_1} + E_{j_2})^2 - (\vec{p}_{j_1} + \vec{p}_{j_2})^2}\,,$$

where $E_{j_{1,2}}$ and $p_{j_{1,2}}$ denote the energy and momentum of the two jets.

The new boson, created through a fusion of two other bosons, decays. One possible channel, that is investigated in this study, is an electron-neutrino pair. This decay equals the decay analysed in the SSM W' search. The electron and neutrino are expected to have a back-to-back signature with, on average, equal amounts of transverse momentum.

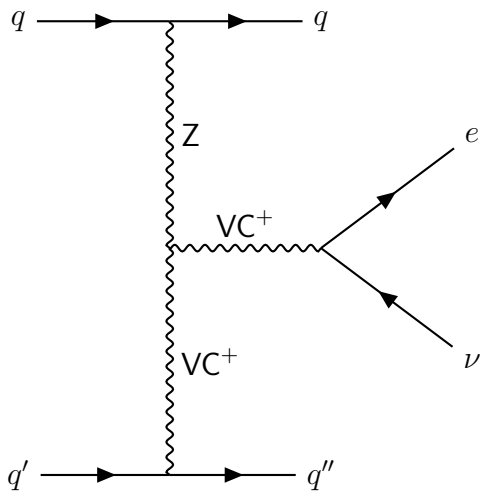

Figure 7.1.: An exemplary Feynman graph for a VBF production of a new charged boson VC.

The study on VBF processes is motivated in consideration of the potentially small possibility for a discovery of a W′ in the context of the SSM. The coupling of the new boson to SM quarks can be small, opening up the case that a W′ boson may have eluded previous searches at the LHC. Couplings to other bosons may, instead, be higher.

7.2. Samples and Selection

In the following, the samples used for this comparing study are presented.

VBF VC samples The samples containing Vector Boson Fusion processes with VC production are produced by Young Do Oh[1] and Christoph Schuler[2] using MadGraph5 and simulating pp-collisions at a centre-of-mass energy 13 TeV. The simulation is based on a model already used in [70]. It particularly provides new heavy bosons of the weak interaction. The samples differ in the generated mass M_{gen} of the VC boson: 600 GeV, 1000 GeV, 1600 GeV, 2000 GeV, and 5000 GeV. In each case, 100 000 events are simulated. The simulations demand $pp \to \mathsf{VC}\,jj$ and $\mathsf{VC} \to e\nu$ processes to be included, where qq are two quarks. This configuration allows – besides other possible processes – for VC producing fusion processes. Quarks are required to be within a $|\eta| < 5.0$ pseudorapidity range and separated with at least $\Delta R = 0.4$ angular distance. VC masses of $M_{\text{gen}} \pm 45 \times$ decay width of VC are allowed. This value is chosen so that no cutoff effects become visible at low or high masses and momenta. Furthermore, no hadronisation of the quarks in the final states to jets is done. In addition, a reconstruction process using detector simulation software is not performed. So, the samples are studied on a pure generator niveau. Since the hadronisation and reconstruction typically do not change particle's flight direction considerably, the notation changes over from "quarks" to "jets" in the subsequent sections.

[1]Kyungpook National University
[2]RWTH Aachen University

SSM W′ samples The samples simulating the $qq \to \mathsf{W}' \to e\nu$ process agree with those used in the first part of this thesis, the SSM interpretation. Mass points are chosen according to the available VBF samples.

Again, it is emphasized that this study is performed on generator level only. For this purpose, the SSM W′ samples are also processed using generator information only.

7.2.1. Selection criteria

The kinematic comparison is done after applying different selection steps. Firstly, the quality cuts described in Section 6.3 are used to exclude low p_T regions and other leptons in the events (with $\vec{p}_T^{\,\nu}$ denoting the transverse momentum of the generated neutrino):

- veto on a second lepton (e, μ, τ) with $p_T > 25\,\text{GeV}$
- $p_T^e > 200\,\text{GeV}$
- $\vec{p}_T^{\,\nu} > 150\,\text{GeV}$

These cuts are applied to both the SSM W′ and the VBF VC signal samples. In addition, VBF specific selection criteria are employed on the VBF VC samples, only, to extract events containing a fusion process of bosons. One requires the invariant mass of the dijet pair (j_1, j_2) in the final state to be greater than 500 GeV. In a second step, a pseudorapidity separation of $|\Delta\eta(j_1, j_2)| > 2.5$ between the two jets is demanded. This due to the expectation of the jets being widely separated from each other in opposing forward regions. These two criteria follow recommendations of Young Do Oh who is a co-author of the VBF Z′ study in [70].

A kinematic selection (such as criteria on $p_T^e/\vec{p}_T^{\,\nu}$ or $\Delta\phi(e, \nu)$) is intentionally omitted. The kinematic distributions will be evaluated considering a possible reviewing of these criteria with respect to VBF processes.

7.3. Comparison: VBF VC and SSM W′

In the following, the two signal types are compared based on kinematic distributions.

7.3.1. Kinematic distributions

Most distributions in the following ground on the $M_{\text{gen}} = 2000\,\text{GeV}$ sample. If not explicitly stated otherwise, statements are also valid for the other mass points. All histograms are normalized to unity in order to compare the two signals on the basis of their shape in kinematic distributions.

Figure 7.2 shows the distribution of the electron and neutrino transverse momenta. In both samples, one can see a peak at 1000 GeV corresponding to the half of the generated mass of 2 TeV. The signals have comparable shapes with a very similar distributed p_T smaller than the peak. Above that the VBF VC signal shows a surplus of about a factor of 2. Electron and neutrino momentum distributions are very akin, matching the expectation of a symmetric two-body decay of the new boson. However, the p_T^e distribution for $M_{\text{gen}} = 5\,\text{TeV}$ in Figure 7.3 shows a difference in the two samples: The p_T^e is nearly uniformly distributed for values below 2.5 TeV, where the SSM W′ signal peaks locally. This observation is also seen in the $\vec{p}_T^{\,\nu}$ variable.

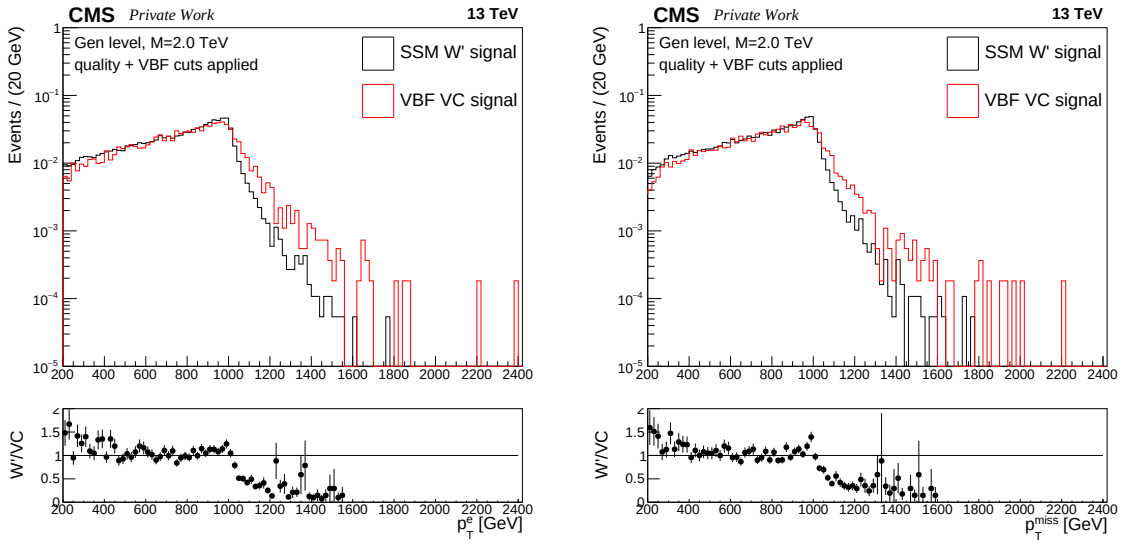

(a) p_T^e distribution.

(b) $\vec{p}_T^{\,\nu}$ distribution.

Figure 7.2.: Comparing distributions of the transverse momenta of electron and neutrino showing the $M_{\text{gen}} = 2000\,\text{GeV}$ SSM W′ (black) and VBF VC (red) signal samples. Underneath, the ratio of both samples in each bin is visualised.

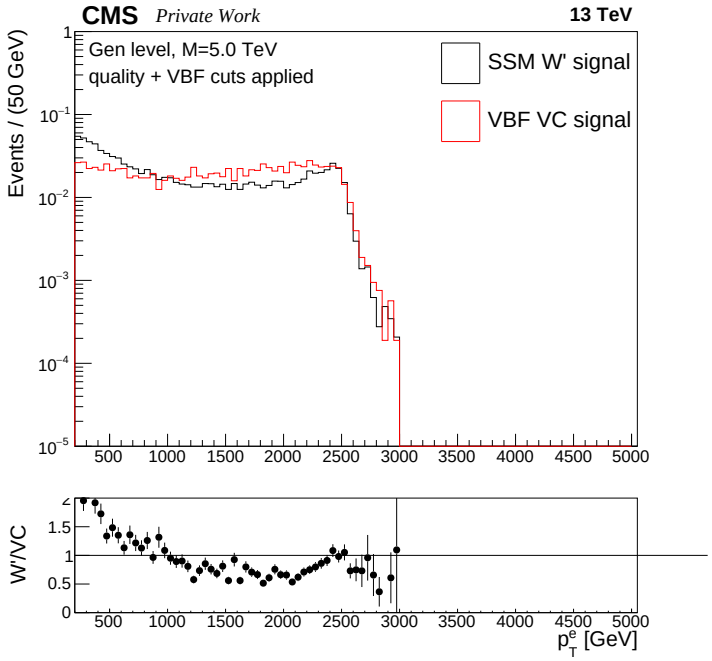

Figure 7.3.: Comparing distribution of the kinematic quantity p_T^e showing the $M_{\text{gen}} = 5000\,\text{GeV}$ SSM W′ (black) and VBF VC (red) signal samples.

Looking at the distribution of the generated mass in Figure 7.4, one can see a similar cumulation around the centre peak at $M_{\text{gen}} = 2000\,\text{GeV}$. The peak is, despite, for the VBF VC signal sharper and, thus, its decay width smaller compared to the SSM W′.

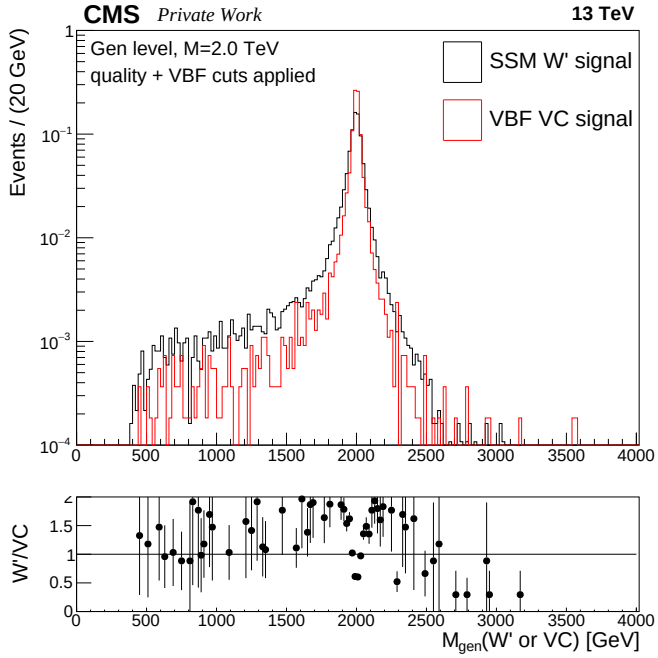

Figure 7.4.: Comparing distribution of the generated mass of the new boson showing the $M_{\text{gen}} = 2000\,\text{GeV}$ SSM W′ (black) and VBF VC (red) signal samples.

The quantities the kinematic selection is applied on in the SSM W′ search are the ratio of p_T^e and $\vec{p}_T^{\,\nu}$ (or p_T^{miss}, on reconstruction level) and the azimuthal angle between the electron and the neutrino, $\Delta\phi(e,\nu)$. Figure 7.5 shows the distributions for these two variables. Again, one can see similarities between the SSM W′ and VBF VC signals. Both samples show a peak at 1 in the p_T^e/p_T^{miss} variable as well as at $\Delta\phi(e,\nu) = \pi \hat{=} 180°$, each corresponding to the two-body decay signature described priorly. However, the peaking behaviour is not that intense for the VBF VC as for the SSM W′ signal. As a consequence, applying the same kinematic selection criteria as in the SSM W′ analysis would cut out more events in the VBF VC samples, relatively speaking. This may lead to lower signal efficiencies. Possibly, a re-optimisation of the criteria for the VBF case is necessary for the purpose of not too low signal efficiencies.

To sum up, one can conclude that – in the basic (leptonic) kinematic quantities – both signal types show some similarities in the distribution shapes. Despite that, differences in the intensities and sharpness of characteristics are observed.

7.3.2. Jets in the VBF signal

In the following, a closer look is taken at the jets contained in the final state of the VBF VC signal samples.

The number of jets in each event equals exactly two, as this is demanded in the

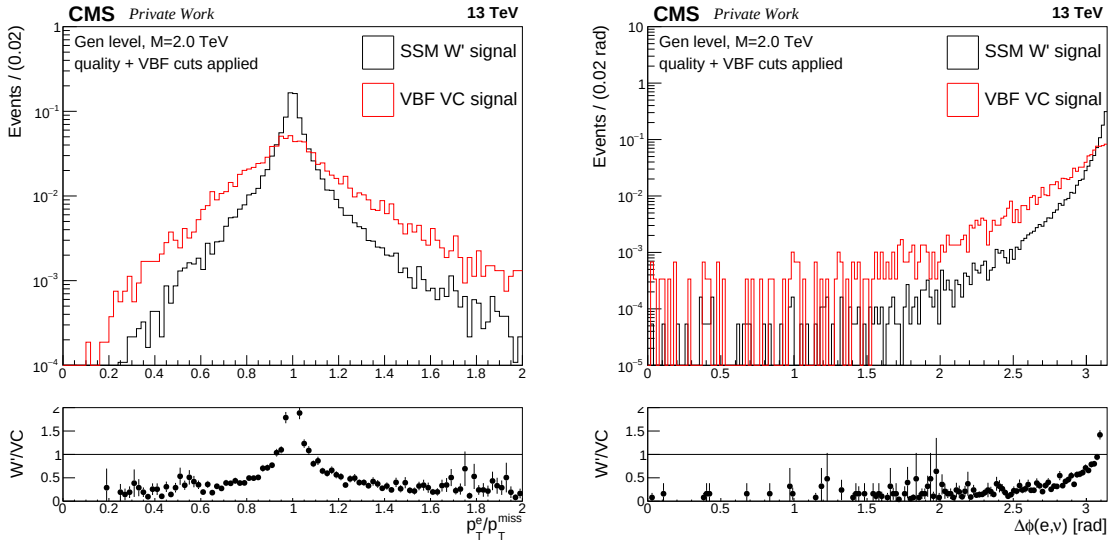

Figure 7.5.: Comparing distributions of the kinematic quantities $p_T^e/\vec{p}_T^{\nu}$ (left) and $\Delta\phi(e,\nu)$ (right) showing the $M_{\text{gen}} = 2000\,\text{GeV}$ SSM W′ (black) and VBF VC (red) signal samples.

simulation process. Each one originates from incoming quarks radiating a boson and – perhaps changed in their flavour – being still present in the final state, as one can see in the Feynman graph in Figure 7.1. The jet transverse momentum distribution is shown in Figure 7.6. The number of events decreases about exponentially with increasing p_T. So, most jets have a low transversal movement.

In accordance with this, as described in Section 7.1, one expects jets in the very forward region. Looking at the jet η distributions in Figure 7.7, this expectation is fulfilled. The most jets are centred around the $\eta = \pm 3$ regions whilst the event count drops in the centre at $\eta = 0$. The peak region corresponds to polar angles of about $\pm\,5.7°$ measured from the beam axis. This forward signature mostly derives from the sub-leading jet as its η distribution has far more distinctive peaks at these regions. The leading jet η shows different behaviour, with the jets not being cumulated in the forward region but nearly equally distributed in a wide range of -2 to 2. However, a slight peaking in the forward region in the leading jet η distribution can be observed in lower mass samples, such as 600 GeV and 1000 GeV. This indicates further underlying processes not being filtered out by the VBF cuts and having predominant effect in the leading jet.

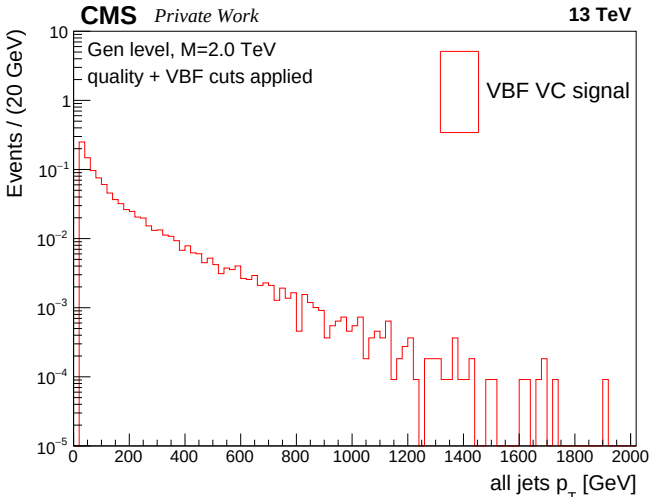

Figure 7.6.: Distribution of the jet p_T showing the $M_{\text{gen}} = 2000\,\text{GeV}$ VBF VC signal sample.

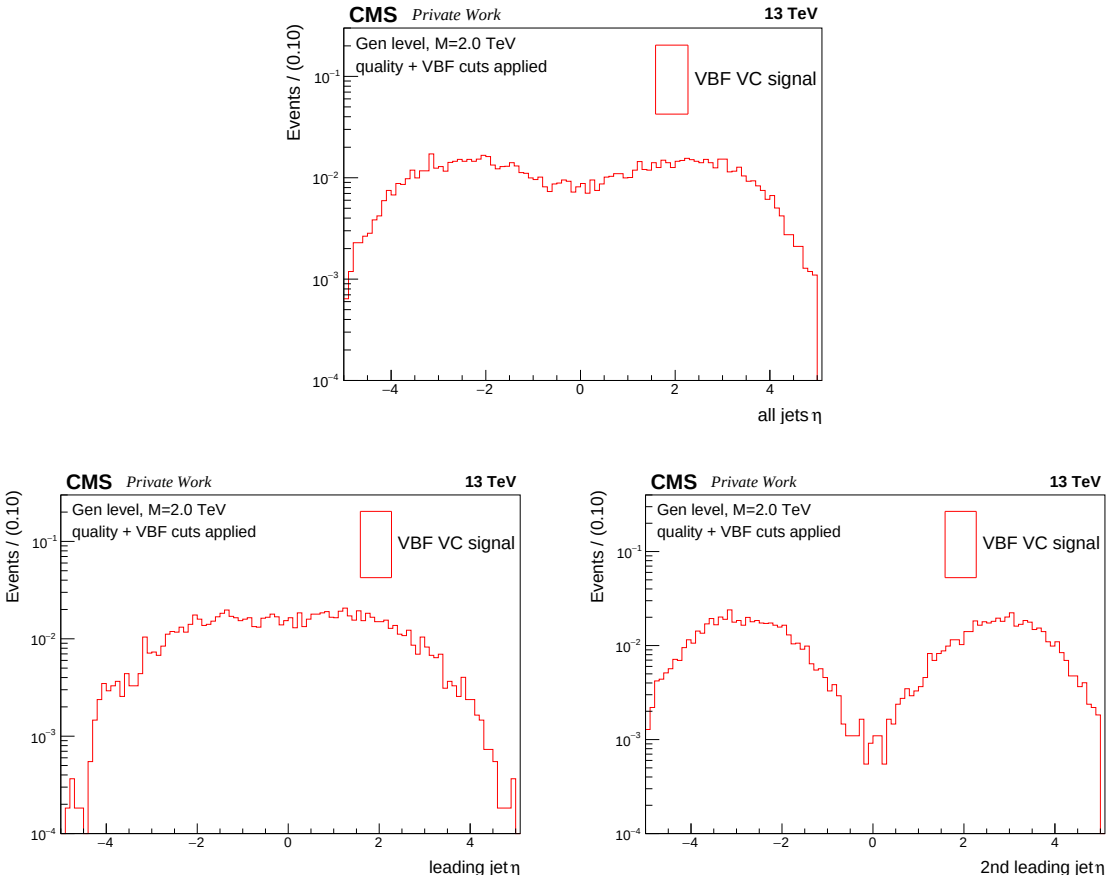

Figure 7.7.: Distributions of the jet η showing the $M_{\text{gen}} = 2000\,\text{GeV}$ VBF VC signal sample. On the top all jets considered, whereas in the lower left and right only the leading (in p_T) or the sub-leading jet, respectively.

7.3.3. Results

Applying the selection stages as described above, including quality and VBF specific cuts, the amount of events falls down to about 5% of the simulated number. This shows that – despite using cuts particularly utilized for the selection of VBF processes – the samples used in this study contain a whole number of other processes. One such possible action is the radiation of gluons from the initial quarks, also resulting in two jets (see Figure 7.8).

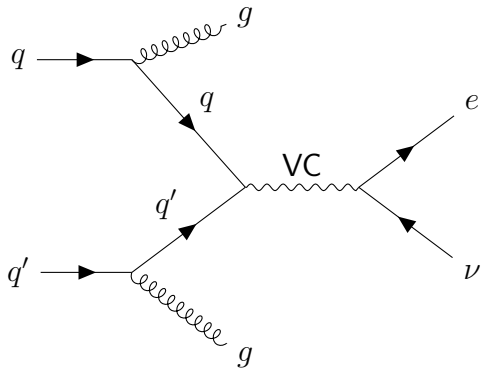

Figure 7.8.: Exemplary Feynman graph leading to the same final state configuration ($jj + e\nu$) as in the designated VBF VC processes. Gluons are radiated by the initial quarks before merging to the new boson VC.

On the one hand, it is not able to extract pure VBF processes. But on the other hand, a cross section calculation targeting VBF VC production and decay is not possible without further ado. Table 7.1 list the cross sections for the SSM W′ and the VBF processes. The latter are values regarding the complete samples and are, thus, unsuitable to draw conclusions about pure VC production through VBF processes.

Table 7.1.: Comparison of cross sections σ for the SSM W′ and complete VBF samples. Conclusions about pure VBF VC production and decay are not possible.

σ/pb	600 GeV	1000 GeV	1600 GeV	2000 GeV	5000 GeV
SSM W′s	25.72	3.03	0.478	0.124	$4.77 \cdot 10^{-4}$
complete VBF sample	0.15004	0.0234	0.00347	0.00123	$2.96 \cdot 10^{-6}$

As one can see, the cross sections are already about two orders of magnitude smaller than those of the SSM W′ production. Cross sections with respect to pure VBF processes are expected to be even smaller, as the used samples contain several other processes. Due to this, one would have to evaluate the sensitivity in available mass regions in further studies. The production of new samples containing a higher fraction of VBF VC production and decay would be gratifying, though this implicates difficulties in MadGraph5 parameter settings.

8. Conclusion and Outlook

A search for new physics with respect to the existence of a new heavy vector boson W' has been performed. The 2017 CMS dataset used in this analysis corresponds to an integrated luminosity of $41.5\,\mathrm{fb}^{-1}$ which is the highest amount of data taken in one year so far. This thesis interprets the data in the context of the Sequential Standard Model, predicting such a new boson with a mass on a TeV scale.

The signal resolution in the transverse mass quantity is calculated and used as the bin width in the corresponding distributions. The resolution moves between 60 and 100 GeV. Data and simulation are in agreement within the statistical and systematical uncertainties. The maximum calculated local significance of deviations is 1.70σ. Thus, no significant excess in data has been observed. An exclusion limit on the W' mass has been set to 4.85 TeV at a confidence level of 95%. The difference of 50 GeV to the corresponding limit set for the 2016 dataset (4.9 TeV) is small.

Regardless of future prospects for sensitivity and limit improvements, the search in this channel allows for constant validation of the data taken with the CMS detector, object reconstruction and possible issues in the $\vec{p}_T^{\,\mathrm{miss}}$ determination.

In addition to the SSM based analysis, a comparing study of Vector Boson Fusion processes that include the production and decay of a new boson VC into the $e\nu$ final state has been performed. Similar kinematic structures have been observed in selected signal samples. Nevertheless, the kinematic selection criteria in $p_T^e/p_T^{\mathrm{miss}}$ and $\Delta\phi(e, \vec{p}_T^{\,\mathrm{miss}})$ need to be reviewed in future studies, as the peaking behaviour is less sharp compared to the SSM W' signal samples. Meeting the expectations, forward jets at $\eta = \pm 3$ are observed. The VBF processes may be the focus of further searches for new heavy vector bosons as soon as pure VBF-like samples are managed to be generated.

A. Appendix

A.1. Cross Section Tables

Table A.1.: Simulated background samples used in the analysis (leptons L = e, μ, τ), their generator, the cross section σ and its order. Taken from [73, 74].

Background		Generator	Order of σ/pb	σ/pb
offshell W boson	WToLNu M-100	Pythia 8.2	LO	163.15
	WToLNu M-200	Pythia 8.2	LO	6.236
	WToLNu M-500	Pythia 8.2	LO	0.2138
	WToLNu M-1000	Pythia 8.2	LO	0.01281
	WToLNu M-2000	Pythia 8.2	LO	5.56e-04
	WToLNu M-3000	Pythia 8.2	LO	2.904e-05
	WToLNu M-4000	Pythia 8.2	LO	3.31e-06
	WToLNu M-5000	Pythia 8.2	LO	2.7e-07
	WToLNu M-6000	Pythia 8.2	LO	1.5e-08
W + jets	WJetsToLNu bulk	MadGraph5	NNLO	61527.5
	WJetsToLNu HT-100To200	MadGraph5	NLO	1632.56
	WJetsToLNu HT-200To400	MadGraph5	NLO	436.604
	WJetsToLNu HT-400To600	MadGraph5	NLO	59.3670
	WJetsToLNu HT-600To800	MadGraph5	NLO	14.6263
	WJetsToLNu HT-800To1200	MadGraph5	NLO	6.67712
	WJetsToLNu HT-1200To2500	MadGraph5	NLO	1.61314
	WJetsToLNu HT-2500ToInf	MadGraph5	NLO	0.03904
top	single top s-channel 4f leptonDecays	aMC@NLO	NLO	3.36
	single top t-channel top 4f inclusiveDecaysV2	Pythia 8.2	NLO	136.02
	single top t-channel antitop 4f inclusiveDecaysV2	Pythia 8.2	NLO	80.95
	single top tW top 5f inclusiveDecays	Pythia 8.2	NNLO	35.85
	single top tW antitop 5f inclusiveDecays	Pythia 8.2	NNLO	35.85
	TTbar	PowHeg	NNLO	831.762

QCD	QCD Pt-50to80	Pythia 8.2	LO	19204300
	QCD Pt-80to120	Pythia 8.2	LO	2762530
	QCD Pt-120to170	Pythia 8.2	LO	471100
	QCD Pt-170to300	Pythia 8.2	LO	117276
	QCD Pt-300to470	Pythia 8.2	LO	7823
	QCD Pt-470to600	Pythia 8.2	LO	648.2
	QCD Pt-600to800	Pythia 8.2	LO	186.9
	QCD Pt-800to1000	Pythia 8.2	LO	32.293
	QCD Pt-1000to1400	Pythia 8.2	LO	9.4183
	QCD Pt-1400to1800	Pythia 8.2	LO	0.84265
	QCD Pt-1800to2400	Pythia 8.2	LO	0.11494
	QCD Pt-2400to3200	Pythia 8.2	LO	0.00683
Drell-Yan	ZToEE M-50to120	PowHeg	NLO	1975
	ZToEE M-120to200	PowHeg	NLO	19.32
	ZToEE M-200to400	PowHeg	NLO	2.731
	ZToEE M-400to800	PowHeg	NLO	0.241
	ZToEE M-800to1400	PowHeg	NLO	0.01678
	ZToEE M-1400to2300	PowHeg	NLO	0.00139
	ZToEE M-2300to3500	PowHeg	NLO	8.948e-5
	ZToEE M-3500to4500	PowHeg	NLO	4.135e-6
	ZToEE M-4500to6000	PowHeg	NLO	4.56e-7
	ZToEE M-6000toInf	PowHeg	NLO	2.066e-8
	GJets HT-40To100	MadGraph5	LO	20790
	GJets HT-100To200	MadGraph5	LO	9238
	GJets HT-200To400	MadGraph5	LO	2305
	GJets HT-400To600	MadGraph5	LO	274.4
	GJets HT-600ToInf	MadGraph5	LO	93.46
Diboson	WWTo4Q	PowHeg	NNLO	51.722
	WWTo2L2Nu	PowHeg	NNLO	12.178
	WWToLNuQQ	PowHeg	NNLO	49.999
	WZTo1L1Nu2Q	aMC@NLO	NLO	10.71
	WZTo2L2Q	aMC@NLO	NLO	5.595
	WZTo1L3Nu	aMC@NLO	NLO	3.033
	WZZ	aMC@NLO	NLO	0.05565
	ZZ	Pythia 8.2	NLO	16.523

Table A.2.: Signal production cross sections (at LO and NNLO) times branching fraction and the corresponding k-factor, for SSM W' bosons decaying into an electron plus neutrino, at $\sqrt{s} = 13\,\text{TeV}$.

$m_{\mathsf{W}'}$ [TeV]	$\sigma_{\text{LO}}\mathcal{B}$ [fb]	$\sigma_{\text{NNLO}}\mathcal{B}$ [fb]	k-factor
0.4	84153	111394	1.324
0.6	19225	25718	1.338
0.8	6494	8717	1.342
1.0	2699.0	3623.5	1.343
1.2	1275.8	1708.9	1.340
1.4	657.28	877.23	1.335
1.6	360.15	478.18	1.328
1.8	206.47	272.38	1.319
2.0	122.55	160.43	1.309
2.2	74.726	96.957	1.298
2.4	46.584	59.813	1.284
2.6	29.560	37.510	1.269
2.8	19.035	23.852	1.253
3.0	12.412	15.348	1.237
3.2	8.1952	9.9844	1.218
3.4	5.4675	6.5682	1.201
3.6	3.6865	4.3708	1.186
3.8	2.5158	2.9432	1.170
4.0	1.7337	2.0092	1.159
4.2	1.2108	1.3926	1.150
4.4	0.85649	0.98188	1.146
4.6	0.61476	0.70621	1.149
4.8	0.44871	0.51886	1.156
5.0	0.33227	0.38928	1.172
5.2	0.25146	0.29832	1.186
5.4	0.19300	0.23371	1.211
5.6	0.15128	0.18659	1.233
5.8	0.12029	0.15148	1.259

A.2. Trigger scale factors

Table A.3.: Trigger scale factors for the combination of the single electron and single photon trigger with their uncertainties. ϵ denotes the trigger efficiency. The table is divided into information on the barrel (EB) and the endcap (EE) region.

η region	electron p_T [GeV]	ϵ_{data}	ϵ_{MC}	$\text{SF} = \epsilon_{\text{data}}/\epsilon_{\text{MC}}$
EB	100-105	$0.000421^{+0.000410}_{-0.000230}$	$0.000552^{+0.000126}_{-0.000103}$	0.76328 ± 0.000429
	105-110	$0.001296^{+0.000639}_{-0.000449}$	$0.000816^{+0.000153}_{-0.000130}$	1.5915 ± 0.000657
	110-120	$0.145305^{+0.003551}_{-0.003481}$	$0.386712^{+0.001678}_{-0.001675}$	0.375745 ± 0.003927
	120-130	$0.817465^{+0.004309}_{-0.004389}$	$0.974507^{+0.000582}_{-0.000595}$	0.83885 ± 0.004429
	130-140	$0.867410^{+0.004302}_{-0.004421}$	$0.984751^{+0.000486}_{-0.000501}$	0.880842 ± 0.004449
	140-150	$0.860892^{+0.004887}_{-0.005033}$	$0.986381^{+0.000491}_{-0.000509}$	0.872778 ± 0.005058
	150-200	$0.884575^{+0.002762}_{-0.002819}$	$0.987492^{+0.000249}_{-0.000254}$	0.89578 ± 0.002831
	200-300	$0.984279^{+0.001501}_{-0.001649}$	$0.999511^{+0.000050}_{-0.000056}$	0.984761 ± 0.001650
	300-400	$0.996587^{+0.001633}_{-0.002691}$	$0.999955^{+0.000022}_{-0.000036}$	0.996632 ± 0.002691
	400-500	$0.996364^{+0.003009}_{-0.008312}$	$0.999978^{+0.000018}_{-0.000050}$	0.996385 ± 0.008313
	500-800	$1^{+0}_{-0.012363}$	$0.999980^{+0.000017}_{-0.000046}$	1.000020 ± 0.012363
	800-2000	$1^{+0}_{-0.184992}$	$1^{+0}_{-0.000011}$	1.000000 ± 0.184993
EE	100-105	$0.001003^{+0.001321}_{-0.000648}$	$0.000612^{+0.000221}_{-0.000168}$	1.64203 ± 0.001339
	105-110	$0.002318^{+0.001829}_{-0.001109}$	$0.001261^{+0.000314}_{-0.000256}$	1.83903 ± 0.001856
	110-120	$0.095683^{+0.005910}_{-0.005609}$	$0.418804^{+0.002720}_{-0.002715}$	0.228468 ± 0.006505
	120-130	$0.684335^{+0.010257}_{-0.010435}$	$0.982191^{+0.000800}_{-0.000836}$	0.696743 ± 0.010469
	130-140	$0.847273^{+0.008941}_{-0.009376}$	$0.992310^{+0.000579}_{-0.000624}$	0.853839 ± 0.009396
	140-150	$0.851111^{+0.009788}_{-0.010328}$	$0.992672^{+0.000619}_{-0.000674}$	0.857394 ± 0.010350
	150-200	$0.864430^{+0.005735}_{-0.005942}$	$0.993668^{+0.000325}_{-0.000342}$	0.869939 ± 0.005952
	200-300	$0.966286^{+0.004215}_{-0.004755}$	$0.999838^{+0.000060}_{-0.000088}$	0.966443 ± 0.004756
	300-400	$0.990826^{+0.004989}_{-0.008844}$	$0.999846^{+0.000100}_{-0.000204}$	0.990979 ± 0.008846
	400-500	$1^{+0}_{-0.023933}$	$1^{+0}_{-0.000394}$	1.000000 ± 0.023937
	500-800	$0.965517^{+0.028544}_{-0.074874}$	$0.999650^{+0.000290}_{-0.000804}$	0.965855 ± 0.074878
	800-2000	1^{+0}_{-0}	$1^{+0}_{-0.007251}$	1 ± 0

Bibliography

[1] Khachatryan, V., ET AL. Search for a heavy gauge boson W ' in the final state with an electron and large missing transverse energy in pp collisions at $\sqrt{s} = 7$ TeV. *Phys. Lett.* B698 (2011), 21–39. DOI: 10.1016/j.physletb.2011.02.048. arXiv: 1012.5945 [hep-ex].

[2] Khachatryan, V., ET AL. Search for physics beyond the standard model in final states with a lepton and missing transverse energy in proton-proton collisions at sqrt(s) = 8 TeV. *Phys. Rev.* D91, 9 (2015), 092005. DOI: 10.1103/PhysRevD.91.092005. arXiv: 1408.2745 [hep-ex].

[3] CMS Collaboration Search for heavy gauge W' bosons in events with an energetic lepton and large missing transverse momentum at $\sqrt{s} = 13\,\text{TeV}$. *Physics Letters B* 770 (2017), 278–301. ISSN: 0370-2693. DOI: https://doi.org/10.1016/j.physletb.2017.04.043.

[4] CMS Collaboration Search for high-mass resonances in final states with a lepton and missing transverse momentum at $\sqrt{s} = 13$ TeV (2018). DOI: 10.1007/JHEP06(2018)128. arXiv: 1803.11133.

[5] Griffiths, D. J. *Introduction to elementary particles*. 2nd rev. ed., 3rd reprint. Physics textbook. OCLC: 711866653. Wiley-VCH, Weinheim, 2010. 454 pp. ISBN: 978-3-527-40601-2.

[6] Einstein, A. Die Grundlage der allgemeinen Relativitätstheorie. *Ann. Phys.* 354 (1916), 769–822. DOI: 10.1002/andp.19163540702.

[7] Fukuda, Y., ET AL. Evidence for Oscillation of Atmospheric Neutrinos. *Phys. Rev. Lett.* 81 (8 Aug. 1998), 1562–1567. DOI: 10.1103/PhysRevLett.81.1562. URL: https://link.aps.org/doi/10.1103/PhysRevLett.81.1562.

[8] Patrignani, C., ET AL. Review of Particle Physics. *Chin. Phys. C* 40, 10 (2016). DOI: 10.1088/1674-1137/40/10/100001.

[9] The CMS collaboration Observation of a new boson at a mass of 125 GeV with the CMS experiment at the LHC. *Physics Letters B* 716, 1 (Sept. 2012), 30–61. ISSN: 03702693. DOI: 10.1016/j.physletb.2012.08.021. URL: http://linkinghub.elsevier.com/retrieve/pii/S0370269312008581 (visited on 08/06/2018).

[10] The ATLAS collaboration Observation of a new particle in the search for the Standard Model Higgs boson with the ATLAS detector at the LHC. *Physics Letters B* 716, 1 (2012), 1–29. ISSN: 0370-2693. DOI: https://doi.org/10.1016/j.physletb.2012.08.020. URL: http://www.sciencedirect.com/science/article/pii/S037026931200857X (visited on 08/06/2018).

[11] Salam, A., AND Ward, J. C. Weak and electromagnetic interactions. *Il Nuovo Cimento (1955-1965)* 11, 4 (Feb. 1959), 568–577. ISSN: 1827-6121. DOI: 10.1007/BF02726525. URL: https://doi.org/10.1007/BF02726525.

[12] Higgs, P. W. Broken Symmetries and the Masses of Gauge Bosons. *Phys. Rev. Lett.* 13 (16 Oct. 1964), 508–509. DOI: 10.1103/PhysRevLett.13.508. URL: https://link.aps.org/doi/10.1103/PhysRevLett.13.508.

[13] Englert, F., AND Brout, R. Broken Symmetry and the Mass of Gauge Vector Mesons. *Phys. Rev. Lett.* 13 (9 Aug. 1964), 321–323. DOI: 10.1103/PhysRevLett.13.321.

[14] Clowe, D., ET AL. A direct empirical proof of the existence of dark matter (2006). DOI: 10.1086/508162. eprint: arXiv:astro-ph/0608407.

[15] Rubin, V. C., AND Ford Jr., W. K. Rotation of the Andromeda Nebula from a Spectroscopic Survey of Emission Regions. *Astrophys. J.* 159 (1970), 379–403. DOI: 10.1086/150317.

[16] Altarelli, G., ET AL. Searching for new heavy vector bosons in $p\bar{p}$ colliders. *Zeitschrift für Physik C Particles and Fields* 47, 4 (Dec. 1, 1990), 676–676. ISSN: 0170-9739, 1431-5858. DOI: 10.1007/BF01552335. URL: https://link.springer.com/article/10.1007/BF01552335.

[17] Olschewski, M. Search for new physics in proton-proton collision events with a lepton and missing transverse energy. Veröffentlicht auf dem Publikationsserver der RWTH Aachen University. Dissertation. RWTH Aachen University, 2016. URL: http://publications.rwth-aachen.de/record/572409.

[18] Herr, W., AND Muratori, B. Concept of luminosity (2006). URL: https://cds.cern.ch/record/941318.

[19] *The Large Hadron Collider | CERN*. URL: https://home.cern/topics/large-hadron-collider (visited on 07/30/2018).

[20] De Melis, C. The CERN accelerator complex. Complexe des accélérateurs du CERN. Jan. 2016. URL: https://cds.cern.ch/record/2119882.

[21] LHC Guide. Mar. 2017. URL: https://cds.cern.ch/record/2255762.

[22] The CMS Collaboration The CMS experiment at the CERN LHC. *Journal of Instrumentation* 3, 08 (2008), S08004. URL: http://stacks.iop.org/1748-0221/3/i=08/a=S08004.

[23] *CMS detector design*. URL: http://cms.web.cern.ch/news/cms-detector-design (visited on 07/31/2018).

[24] Bayatyan, G. L., ET AL. *CMS TriDAS project: Technical Design Report, Volume 1: The Trigger Systems*. Technical Design Report CMS. URL: http://cds.cern.ch/record/706847.

[25] Cittolin, S., ET AL. *CMS The TriDAS Project: Technical Design Report, Volume 2: Data Acquisition and High-Level Trigger. CMS trigger and data-acquisition project*. Technical Design Report CMS. CERN, Geneva, 2002. URL: http://cds.cern.ch/record/578006.

[26] Khachatryan, V., ET AL. The CMS trigger system. *JINST* 12, 01 (2017), P01020. DOI: 10.1088/1748-0221/12/01/P01020. arXiv: 1609.02366.

[27] Sirunyan, A. M., ET AL. Particle-flow reconstruction and global event description with the CMS detector. *JINST* 12, 10 (2017), P10003. DOI: 10.1088/1748-0221/12/10/P10003. arXiv: 1706.04965 [physics.ins-det].

[28] The CMS Collaboration *IntroToJEC < CMS < TWiki*. URL: https://twiki.cern.ch/twiki/bin/view/CMS/IntroToJEC (visited on 07/31/2018).

[29] The CMS Collaboration *JetEnergyScale < CMS < TWiki*. URL: https://twiki.cern.ch/twiki/bin/viewauth/CMS/JetEnergyScale (visited on 08/02/2018).

[30] The CMS Collaboration *Egamma2017DataRecommendations < CMS < TWiki*. URL: https://twiki.cern.ch/twiki/bin/viewauth/CMS/Egamma2017DataRecommendations (visited on 08/09/2018).

[31] The CMS Collaboration *Good Luminosity Section Files from CMS*. URL: https://cms-service-dqm.web.cern.ch/cms-service-dqm/CAF/certification/Collisions17/13TeV/ (visited on 07/22/2018).

[32] The CMS Collaboration *PdmV2017Analysis < CMS < TWiki*. URL: https://twiki.cern.ch/twiki/bin/viewauth/CMS/PdmV2017Analysis (visited on 08/20/2018).

[33] The CMS Collaboration *The CMS Offline WorkBook < CMSPublic < TWiki*. URL: https://twiki.cern.ch/twiki/bin/view/CMSPublic/WorkBook (visited on 08/01/2018).

[34] Sjöstrand, T., ET AL. An Introduction to PYTHIA 8.2. *Comput. Phys. Commun.* 191 (2015), 159–177. DOI: 10.1016/j.cpc.2015.01.024. arXiv: 1410.3012 [hep-ph].

[35] Alwall, J., ET AL. MadGraph 5 : Going Beyond. *JHEP* 06 (2011), 128. DOI: 10.1007/JHEP06(2011)128. arXiv: 1106.0522 [hep-ph].

[36] Alioli, S., ET AL. A general framework for implementing NLO calculations in shower Monte Carlo programs: the POWHEG BOX. *JHEP* 06 (2010), 043. DOI: 10.1007/JHEP06(2010)043. arXiv: 1002.2581 [hep-ph].

[37] Frixione, S., ET AL. Matching NLO QCD computations with Parton Shower simulations: the POWHEG method. *JHEP* 11 (2007), 070. DOI: 10.1088/1126-6708/2007/11/070. arXiv: 0709.2092 [hep-ph].

[38] CMS Collaboration Cross section calculation for leptonically decaying W at NNLO QCD and NLO electroweak. CMS Internal CMS-AN-2014/263. 2014.

[39] Alioli, S., ET AL. NLO single-top production matched with shower in POWHEG: s- and t-channel contributions. *JHEP* 09 (2009), 111. DOI: 10.1007/JHEP02(2010)011,10.1088/1126-6708/2009/09/111. arXiv: 0907.4076 [hep-ph].

[40] Re, E. Single-top Wt-channel production matched with parton showers using the POWHEG method. *Eur. Phys. J.* C71 (2011), 1547. DOI: 10.1140/epjc/s10052-011-1547-z. arXiv: 1009.2450 [hep-ph].

[41] Campbell, J. M., ET AL. Top-Pair Production and Decay at NLO Matched with Parton Showers. *JHEP* 04 (2015), 114. DOI: 10.1007/JHEP04(2015)114. arXiv: 1412.1828 [hep-ph].

[42] Alwall, J., ET AL. The automated computation of tree-level and next-to-leading order differential cross sections, and their matching to parton shower simulations. *JHEP* 07 (2014), 079. DOI: 10.1007/JHEP07(2014)079. arXiv: 1405.0301 [hep-ph].

[43] Consonni, C. Study of electron fake rate from QCD jets in CMS ECAL calorimeter. 2008. URL: http://disi.unitn.it/~consonni/publications/files/BSc_thesis_Cristian_Consonni.pdf.

[44] Quackenbush, S., ET AL. W physics at the LHC with FEWZ 2.1. *Computer Physics Communications* 184, 1 (2013), 209–214. ISSN: 0010-4655. DOI: https://doi.org/10.1016/j.cpc.2012.09.005. URL: http://www.sciencedirect.com/science/article/pii/S0010465512002913.

[45] CMS Collaboration PDF Uncertainties and K-factor Calculations for the SSM W' at 13 TeV Collisions. CMS Internal CMS-AN-2014/240. 2014.

[46] The CMS Collaboration *MissingETOptionalFilters < CMS < TWiki*. URL: https://twiki.cern.ch/twiki/bin/viewauth/CMS/MissingETOptionalFilters (visited on 08/04/2018).

[47] The CMS Collaboration *MissingETOptionalFiltersRun2 < CMS < TWiki*. URL: https://twiki.cern.ch/twiki/bin/viewauth/CMS/MissingETOptionalFiltersRun2 (visited on 08/04/2018).

[48] The CMS Collaboration *Symbols, units, particle names < Guidelines for the general style of CMS publications < CMS Guidelines for Authors < CMSInternal < TWiki*. URL: https://twiki.cern.ch/twiki/bin/view/CMS/Internal/PubGuidelines (visited on 08/04/2018).

[49] Halil Saka *HCAL Noise and Noise Filters in 2016 at Run Organization Meeting: Calorimeters Data Jamboree (27 May 2016) on Indico*. URL: https://indico.cern.ch/event/534040/ (visited on 08/04/2018).

[50] The CMS Collaboration *SusyEcalMaskedCellSummary < CMS < TWiki*. URL: https://twiki.cern.ch/twiki/bin/view/CMS/SusyEcalMaskedCellSummary (visited on 08/04/2018).

[51] Isabell Melzer-Pellmann *Report from the MET Scanners at PPD General Meeting (1 December 2016) on Indico*. URL: https://indico.cern.ch/event/591506/ (visited on 08/04/2018).

[52] Laurent Thomas *2016 Beam Halo Filter Update at MET Working Group Meeting (27 April 2016) on Indico*. URL: https://indico.cern.ch/event/518559/ (visited on 08/04/2018).

[53] The CMS Collaboration *HEEPElectronIdentificationRun2 < CMS < TWiki*. URL: https://twiki.cern.ch/twiki/bin/view/CMS/HEEPElectronIdentificationRun2?rev=28 (visited on 08/02/2018).

[54] The CMS Collaboration *HEEPElectronID < CMS < TWiki*. URL: https://twiki.cern.ch/twiki/bin/viewauth/CMS/HEEPElectronID (visited on 08/02/2018).

[55] The CMS Collaboration Search for new physics in the lepton and MET final state with 2016 data. CMS Internal CMS-AN-2016/204. 2016.

[56] *GitHub - cms-sw/cmssw: CMS Offline Software*. URL: https://github.com/cms-sw/cmssw (visited on 08/08/2018).

[57] *GitLab - aachen-3a / tapas*. CMS Internal. URL: https://gitlab.cern.ch/aachen-3a/tapas (visited on 08/08/2018).

[58] Bretz, H.-P., ET AL. A development environment for visual physics analysis. *Journal of Instrumentation* 7, 08 (2012), T08005. URL: http://stacks.iop.org/1748-0221/7/i=08/a=T08005.

[59] The CMS Collaboration *PileupJSONFileforData < CMS < TWiki*. URL: https://twiki.cern.ch/twiki/bin/viewauth/CMS/PileupJSONFileforData (visited on 08/11/2018).

[60] *Hypernews: Recommended cross section for pile-up reweigthing*. URL: https://hypernews.cern.ch/HyperNews/CMS/get/luminosity/613/2/1/1/1.html (visited on 08/11/2018).

[61] The CMS Collaboration *TWikiLUM < CMS < TWiki*. URL: https://twiki.cern.ch/twiki/bin/viewauth/CMS/TWikiLUM (visited on 08/15/2018).

[62] The CMS Collaboration *JECDataMC < CMS < TWiki*. URL: https://twiki.cern.ch/twiki/bin/view/CMS/JECDataMC (visited on 08/16/2018).

[63] Butterworth, J., ET AL. PDF4LHC recommendations for LHC Run II (2015). DOI: 10.1088/0954-3899/43/2/023001. arXiv: 1510.03865.

[64] *MUSiC, a Model Unspecific Search for New Physics, in pp Collisions at* $\sqrt{s} =$ 8 TeV. Tech. rep. CMS-PAS-EXO-14-016. Geneva: CERN, 2017. URL: http://cds.cern.ch/record/2256653.

[65] Read, A. L. Modified frequentist analysis of search results (the CL_s method). CERN-OPEN-2000-205 (2000). URL: http://cds.cern.ch/record/451614 (visited on 08/20/2018).

[66] The CMS Collaboration *SWGuideHiggsAnalysisCombinedLimit < CMS < TWiki*. URL: https://twiki.cern.ch/twiki/bin/viewauth/CMS/SWGuideHiggsAnalysisCombinedLimit (visited on 08/21/2018).

[67] *HiggsAnalysis-CombinedLimit: CMS Higgs Combination toolkit*. original-date: 2013-06-21T15:34:08Z. URL: https://github.com/cms-analysis/HiggsAnalysis-CombinedLimit (visited on 08/21/2018).

[68] The CMS Collaboration *WebHome < RooStats < TWiki*. URL: https://twiki.cern.ch/twiki/bin/view/RooStats/WebHome (visited on 08/21/2018).

[69] Kilian, W., ET AL. *Multi-Higgs Production and Unitarity in Vector-Boson Fusion at Future Hadron Colliders*. 2018. arXiv: 1808.05534.

[70] Andres, F., ET AL. Searching for New Heavy Neutral Gauge Bosons using Vector Boson Fusion Processes at the LHC (2016). DOI: 10.1016/j.physletb.2017.01.062. eprint: arXiv:1609.09765.

[71] Delannoy, A. G., ET AL. Probing Dark Matter at the LHC using Vector Boson Fusion Processes (2013). DOI: 10.1103/PhysRevLett.111.061801. arXiv: 1304.7779.

[72] Dutta, B., ET AL. Vector Boson Fusion Processes as a Probe of Supersymmetric Electroweak Sectors at the LHC (2012). DOI: 10.1103/PhysRevD.87.035029. arXiv: 1210.0964.

[73] *Aachen 3A DB < CMSInternal*. URL: https://cms-project-aachen3a-db.web.cern.ch/index (visited on 08/01/2018).

[74] The CMS Collaboration *Summary table of samples produced for the 1 Billion campaign, with 25ns bunch-crossing < CMS < TWiki*. URL: https://twiki.cern.ch/twiki/bin/viewauth/CMS/SummaryTable1G25ns (visited on 08/01/2018).